

Fatigue life prediction methodology for L-flange connection under different preload levels based on crack growth analysis

Shakeri, Iman; El Bamby, Hagar; Tankova, Trayana; Velikovic, Milan

10.1016/j.tws.2025.113893

Publication date

Document Version Final published version

Published in Thin-Walled Structures

Citation (APA)

Shakeri, I., El Bamby, H., Tankova, T., & Veljkovic, M. (2025). Fatigue life prediction methodology for Lflange connection under different preload levels based on crack growth analysis. Thin-Walled Structures, 217, Article 113893. https://doi.org/10.1016/j.tws.2025.113893

Important note

To cite this publication, please use the final published version (if applicable). Please check the document version above.

Copyright

Other than for strictly personal use, it is not permitted to download, forward or distribute the text or part of it, without the consent of the author(s) and/or copyright holder(s), unless the work is under an open content license such as Creative Commons.

Please contact us and provide details if you believe this document breaches copyrights. We will remove access to the work immediately and investigate your claim.

ELSEVIER

Contents lists available at ScienceDirect

Thin-Walled Structures

journal homepage: www.elsevier.com/locate/tws





Fatigue life prediction methodology for L-flange connection under different preload levels based on crack growth analysis

Iman Shakeri*, Hagar El Bamby, Trayana Tankova, Milan Veljkovic

Department of Engineering Structures, Delft University of Technology, 2628CN Delft, The Netherlands

ARTICLE INFO

Keywords:
Fatigue life
S-N curve
Fatigue crack growth
Bolted flange connection
Preload
Stress intensity factor

ABSTRACT

Bolted flange connections in wind turbine towers are subjected to cyclic loading, making fatigue a critical concern for their structural integrity. Bolt preload helps mitigate fatigue damage, but actual preload levels often deviate from design values due to uncertainties in the tightening process and geometric imperfections. This study evaluates the fatigue life of bolts L-flange connections under varying preload levels using a numerical fracture mechanics approach. A comprehensive three-dimensional finite element analysis (FEA) is conducted to assess the effects of preload on the stress intensity factor (SIF), crack propagation behaviour, and load transfer function (LTF). Additionally, the influence of thread helix angle, as well as combined axial and bending loads, on SIF and crack front evolution is examined. Experimental validation of the numerically obtained LTF is performed. A methodology for predicting S-N curves is proposed by deriving normalised solutions for LTF and SIF. The results indicate that increasing preload up to 90 % significantly reduces the SIF range, thereby decelerating crack growth and enhancing fatigue life. However, beyond 90 %, the improvement in fatigue life becomes less pronounced. Furthermore, the findings suggest that Eurocode 3 provides conservative fatigue life predictions, as it neglects bending effects, which are less detrimental than axial loading. Notably, even minor preload loss considerably shortens fatigue life, an effect that becomes more pronounced at higher preload levels. This research contributes to the development of predictive fatigue models for the bolted L-flange connection, providing insights into incorporating preload effects into fatigue life assessments.

1. Introduction

The increasing global demand for renewable energy has driven advancements in wind turbine technology, with offshore wind farms playing a crucial role in sustainable power generation. A critical component in wind turbine support structures is the bolted L-flange connection, which serves to join tower segments and transmit complex loads generated during operation [1], as illustrated in Fig. 1a. These connections are subjected to cyclic axial and bending loads, making them susceptible to fatigue failure. A comprehensive understanding of their fatigue behaviour is essential to ensure structural integrity, optimise design, and improve long-term reliability, particularly under varying preload conditions and dynamic loads. The fatigue behaviour of L-flange connections is primarily governed by the bolt preload level, stress concentration at the thread roots, load eccentricity leading to combined axial and bending stresses and geometric imperfections.

Preload in a bolted connection refers to the initial tensile force

applied to the bolt during tightening, which induces a clamping force between connected components, as shown in Fig. 1b. This force allows external loads to be primarily transferred through friction at the interface rather than through the bolt itself, thereby reducing stress fluctuations under cyclic loading. As a result, preload serves as a key factor in mitigating fatigue failure by minimising stress amplitude variations and preventing loosening due to dynamic effects.

The load transfer function (LTF) describes the relationship between the external force acting on the tower shell, F_{ext} , and the force experienced by the bolt, F_b , as shown schematically in Fig. 1c. Under ideal geometric conditions, flange tightening increases surface pressure between the mating faces, leading to a centric clamp force around the longitudinal bolt axis, which acts as a counterpart to the preload, as depicted in Fig. 1b. Due to the combined effects of preload and load eccentricity, the transfer of external loads to the bolt follows a nonlinear pattern [2]. In cases where a symmetric clamp force exists around the bolt axis, external forces initially reduce the clamp load before being fully transmitted to the bolt.

E-mail addresses: I.Shakeri-1@tudelft.nl, iman.shakeri1368@gmail.com (I. Shakeri), H.ElBamby@tudelft.nl (H. El Bamby), T.Tankova@tudelft.nl (T. Tankova), M.Veljkovic@tudelft.nl (M. Veljkovic).

^{*} Corresponding author.

Nomenclature			Material parameter in NASGRO equation
		N_f	Number of cycles to failure
Α	Constant of S-N curve	Nut_{Free}	Free nut rotation
а	Crack depth	\boldsymbol{P}	Thread pitch
$A_{\rm s}$	Stud cross section	p	Material parameter in NASGRO equation
A_t	Tensile-stress area	q	Material parameter in NASGRO equation
a_0	Intrinsic crack length	R	Stud radius
a_c	Critical crack length	R_{ext}	External load ratio
a_i	Initial crack length	R_B	Load ratio of the stud
b	Arc half-length of the crack	S	Standard deviation
C	Material parameter in NASGRO equation	S_u	Ultimate Strength
c	Crack half-length	S_{y}	Yield Stress
C_{th}	Empirical constant	t_l	One-sided tolerance limit factor
D	Stud nominal diameter	$W_{ m f}$	Flange width
D_{major}	Stud major diameter	$Y_{ m B}$	Dimensionless stress intensity factor for bending
D_{minor}	Stud minor diameter	Y_{A}	Dimensionless stress intensity factor for axial force
DC_{mean}	Mean detail category	α	Constraint factor
DC_{Table}	Design (characteristic) detail category	γ	Crack opening function
E	Young's modulus	γ_{M}	Adjustment factor from design to mean curve
F_B	Internal stud force	$\Delta K_{ m I,th}$	Threshold stress intensity factor range
$F_{B,trans}$	Portion of external load transferred to the stud	$\Delta K_{ ext{th,0}}$	Threshold stress intensity factor range at $R_B = 0$
F_{ext}	External force applied to the flange	ΔNut	Effective nut rotation
F_{PL}	Stud force caused by preload	ΔS_{axial}	Axial stress range in the stud
F_u	Ultimate strength of the stud	ΔS_{ext}	External stress range applied to the flange
F_{y}	Yield force of the stud	$\Delta S^{ m nom}$	nominal stress range
I	Second-area moment	$arepsilon_e$	Engineering strain
$J_{ m int}$	Interaction integral	$arepsilon_t$	True strain
K_{C}	Critical stress intensity factor	θ	Angle of strain gauge in regards to x' axis
K_{I}	Stress intensity factor of mode I	σ_A	Axial stress
K_{II}	Stress intensity factor of mode II	σ_B	Bending stress
$K_{ m III}$	Stress intensity factor of mode III	σ_e	Engineering stress
k_s	Size factor	σ_F	Flow stress
L	Stud length	σ_t	True stress
$L_{\rm c}$	Contact length	λ	Plane strain/stress factor
M	Bending moment	ν	Poisson's ratio
m	Inverse slope of S-N curve		
N	Number of cycles		

Several studies have investigated the role of preload in bolted flange connections. Schaumann and Seidel [3] examined failure modes in bolted steel flanges, emphasising the importance of precise preload application for effective load transfer and fatigue performance. Seidel [5] and Seidel & Schaumann [6] analysed fatigue loads in ring flange connections, highlighting the critical role of bolt preload in distributing operational stresses. Mehmanparast et al. [1] reviewed fatigue challenges in offshore wind turbine bolted connections, identifying preload optimisation as a key strategy for mitigating premature failures. Although high preload application causes measurable plastic deformation [7], studies have reported that this does not compromise the joint's structural integrity [8], as its effect on ultimate load capacities is generally insignificant [9]. Shahani and Shakeri [10] experimentally investigated the effect of preload on the endurance limit of bolts under pure axial loading. Their results demonstrated that the high mean stress resulting from increased preload levels does not reduce the endurance limit due to localised plasticity at the thread roots. Glienke et al. [11] and Maljaars and Euler [12] have studied the impact of mean stress on bolt fatigue life, noting variations in fatigue properties across different standards due to insufficient design guidelines for bolts with different materials and assemblies [13], as well as the limited available data on high mean stress levels [12].

In practice, the actual preload in bolts often deviates from design specifications due to uncertainties in the tightening process, geometric imperfections [14], or improper installation. These deviations increase

stress fluctuations, leading to accelerated fatigue damage [15,16]. Additionally, preload loss over time is commonly observed due to settlements, prolonged vibrations, cyclic loading, or plastic strain accumulation in the bolt and flange [17]. However, there is no information available in existing fatigue prediction standards, such as Eurocode 3 [18] and DNV-RP-203 [19], especially about the lack of preload loss and explicit influence of bending interaction in L-flange connections. The newest results about geometric imperfection of L-flanges, preload loss and bolt force and moment calculation model are included in IEC 61400-6 [17]. Therefore, understanding the extent to which preload loss affects fatigue life is essential for improving bolted connection design and developing accurate predictive models.

While standards such as Eurocode 3 [18] provide baseline fatigue life predictions for bolted connections, their conservative nature often leads to an underestimation of fatigue life, as they do not account for the bending loads in flange connections caused by eccentricity [20]. Lochan et al. [21] reviewed the fatigue performance of bolted connections in offshore wind turbines, highlighting the limitations of current standards and the need for more comprehensive fatigue models. Schwarz et al. [22] experimentally demonstrated that neglecting the bending effect on the stress range in L-flanges leads to a significantly shorter fatigue life prediction when using fatigue data from axially loaded bolt-nut connections. These studies underscore the importance of considering load transfer mechanisms when predicting flange connection fatigue life.

Numerical simulations have contributed significantly to

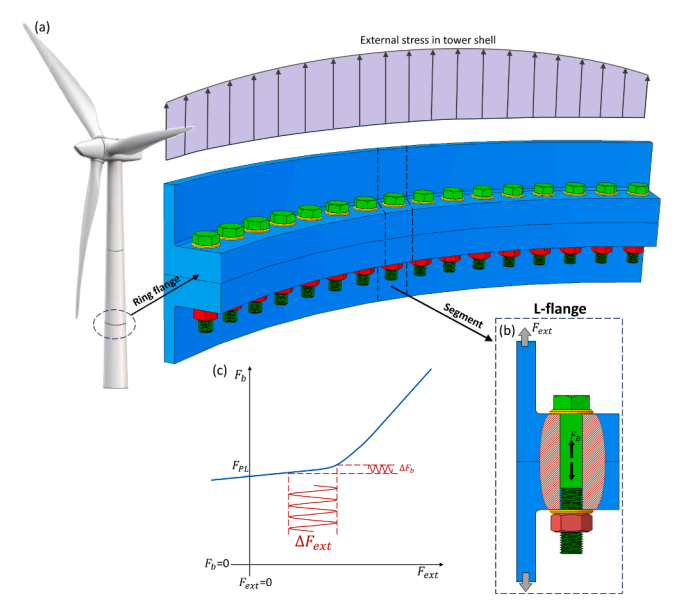


Fig. 1. (a) Typical ring flange connection in a wind turbine tower (adopted from [3]) (b) L-flange connection, (c) Load transfer mechanism under perfect geometric conditions (adapted from [4]).

understanding the structural integrity and fatigue performance of bolted connections in wind turbines [23-27]. Global methods, such as the S-N approach used in standards, do not explicitly consider key factors such as actual bolt geometry, stress redistribution due to cracking, loss of bolt pretension, and changes in loading conditions, emphasising the need for advanced methods to ensure reliable fatigue and structural assessment [28,29]. Okorn et al. [30,31] examined the influence of geometric imperfections in preloaded flange connections using finite element analysis (FEA), highlighting their impact on fatigue loads and bolt integrity. However, their model did not account for detailed bolt geometry. Yang et al. [32] studied tensile loading effects on damage initiation using fracture simulations that incorporated detailed thread geometry. Wegener et al. [33,34] analysed ring flange connections and numerically evaluated preload loss due to high single loads and plastic deformation in the flange or bolt. Cheng et al. [35,36] conducted detailed FEA of ring flange connections, identifying critical stress distributions and deformation patterns under varying loading conditions. These studies demonstrate the effectiveness of FEA in capturing complex interactions between preload and cyclic loading, thereby aiding design optimisation and predictive maintenance strategies.

An important aspect of fatigue analysis in bolted connections is the characterisation of crack propagation. Annoni et al. [37] examined fatigue life in threaded connections for offshore wind turbines, demonstrating that accurate modelling of crack propagation is pivotal for understanding the fatigue behaviour of bolted joints. Stranghöner et al. [38] and Zhang et al. [39] performed fracture mechanics-based analyses to evaluate crack propagation in high-strength bolts, revealing the influence of parameters such as bolt diameter and initial crack location on stress intensity factor (SIF) and fatigue life. Eichstädt [40] investigated fatigue assessment methods for large-size bolted assemblies, demonstrating the interplay between bolt geometry, material properties, and preload levels in determining fatigue resistance of wind turbine support structures. However, research on the impact of varying preload levels on fatigue crack propagation using detailed modelling remains limited.

Based on the author's research and the state-of-the-art study, the following key research gaps in the fatigue assessment of L-flange connections have been identified: (i) the effect of bending caused by load eccentricity on fatigue behaviour and crack propagation, (ii) the influence of preload loss on fatigue life, and (iii) the lack of SIF solutions for an equivalent 3D semi-elliptical crack subjected to combined axial-

bending loading in a bolted connection, considering realistic thread geometry. This study addresses these gaps by evaluating the fatigue life of bolts in L-flange connections under varying preload levels utilising a fracture mechanics approach. A comprehensive three-dimensional fracture mechanics analysis is performed on an L-flange connection subjected to different preload levels and external loads. To predict the fatigue life of bolted connections using a fracture mechanics approach, both LTF and SIF should be determined. Prediction fatigue models based on fracture mechanics are used in welded connections but not so frequently in bolted connections. To address this gap, the study systematically examines the effects of preload on crack propagation, SIF ranges, and LTF, while also assessing the impact of thread helix angle and combined axial and bending loads on SIF and crack front evolution. The LTF obtained from numerical simulations, which account for preload effects, is validated against experimental data. The results demonstrate that preload significantly influences crack growth, SIF range, and fatigue life, ultimately affecting the associated S-N curves. By deriving normalised solutions for LTF and SIF, a methodology for predicting S-N curves is proposed. The novel findings of normalised solutions for LTF and SIF contribute to the development of fracture mechanics in L-flange connections, enabling their application to a wider range of axial-bending loading scenarios and supporting improved design guidelines that enhance the long-term reliability of L-flange connections in wind turbine towers.

2. Models and Methods

This section presents the methodology for predicting the fatigue life of an L-flange bolted connection subjected to various preload levels, involving a sequence of numerical analysis steps. It begins with an overview of the geometry and material properties used in the case study, followed by a description of the finite element (FE) model developed to simulate preload application. The modelling approach for fatigue crack growth (FCG) and fatigue life prediction is then detailed, and finally, the procedure for constructing the S-N diagram is described.

2.1. The considered L-flange connection

An L-flange connection, shown in Fig. 2a, was modelled using ABAQUS 2023 [41]. The M48 partially threaded stud and ISR nut, both of class 10.9 with a 5 mm pitch, were modelled with threads featuring a tolerance class of 6g and 6H, respectively, according to ISO 965-1 [42]. The major and minor diameters of the stud are 47.7 mm and 41.9 mm, while those of the nut are 48.5 mm and 42.9 mm. The stud includes a 112 mm long unthreaded section with a diameter of 45 mm, and the nut has an outer diameter of 92 mm.

All parts were assigned a modulus of elasticity of E=210 GPa and Poisson's ratio ν =0.3. The flange, stud, and nut were modelled with elastic-plastic material behaviour with isotropic hardening. The flange was assumed to be made of steel grade S355, with material properties taken from the Swedish design handbook BSK07 [43]. For the 10.9-class bolt and nut, a parabolic engineering stress-strain curve was assumed for the pre-necking plastic region [44]. Since the numerical analysis requires the true stress-strain relationship as input, the pre-necking engineering stress-strain curves for the various components were converted into pre-necking true stress-strain curves using the following equations:

$$\varepsilon_t = \ln(1 + \varepsilon_e) \tag{1}$$

$$\sigma_t = \sigma_e(1 + \varepsilon_e) \tag{2}$$

where the subscripts t and e denote true and engineering values, respectively. Fig. 2b shows the true stress-strain curves up to the ultimate strength for the L-flange, stud, and nut in the pre-necking region.

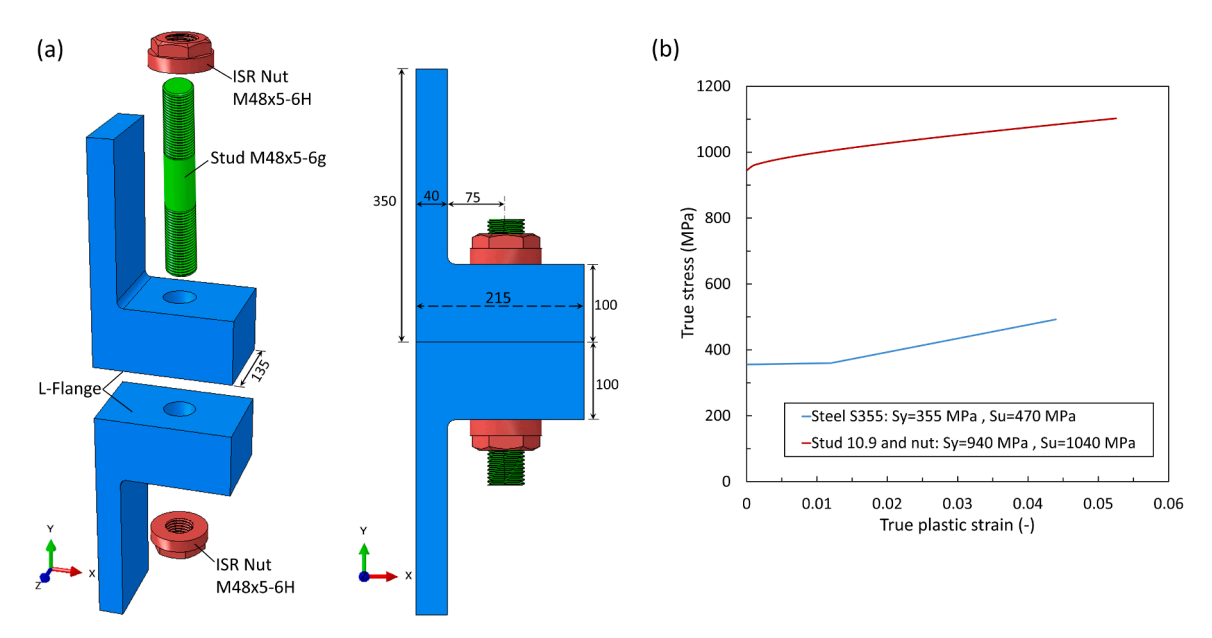


Fig. 2. (a) Exploded (left) and assembled (right) views of an L-flange connection featuring an M48 stud and nut. (b) Nominal pre-necking true stress-strain curves of the L-flange, stud and nut.

2.2. The FE model of preload application

First, a global model of the L-flange was created in ABAQUS. In Step 1, preload was applied using the turn-of-nut method. The hexagonal edges of the lower nut were coupled to a reference point at its centreline via a kinematic (rigid) coupling constraint. Various rotation angles were applied to the lower nut to achieve different preloading forces in the stud, while the upper nut was kept fixed and merged with the stud for computational efficiency (Fig. 3a).

General contact was defined for all interactions, including flange-to-flange, nut-to-flange, and stud-to-nut threads. Normal behaviour was modelled using hard contact, while tangential behaviour was defined using a penalty friction formulation with a friction coefficient of 0.2, which is commonly used for steel-on-steel threaded interfaces [45]. Sensitivity studies conducted in Refs. [39,46] have shown that the

friction coefficient between threads has minimal influence on the mode I SIF for a crack length of 1 mm. Due to contact nonlinearity, an explicit method with nonlinear geometry effects was used.

The stud and nut were meshed with quadratic tetrahedral elements (C3D10M), while the flanges were meshed with eight-node hexagonal elements (C3D8R) with reduced integration and hourglass control. In Step 2, after preload application, an external load F_{ext} was applied to the top flange, while the bottom surface of the lower flange was fixed (Fig. 3a).

2.3. FCG simulation

To determine the fatigue life of the stud using a fracture mechanics approach, a three-dimensional FCG simulation was performed using ABAQUS 2023 [41] and ZENCRACK 9.3-1 [47] commercial software.

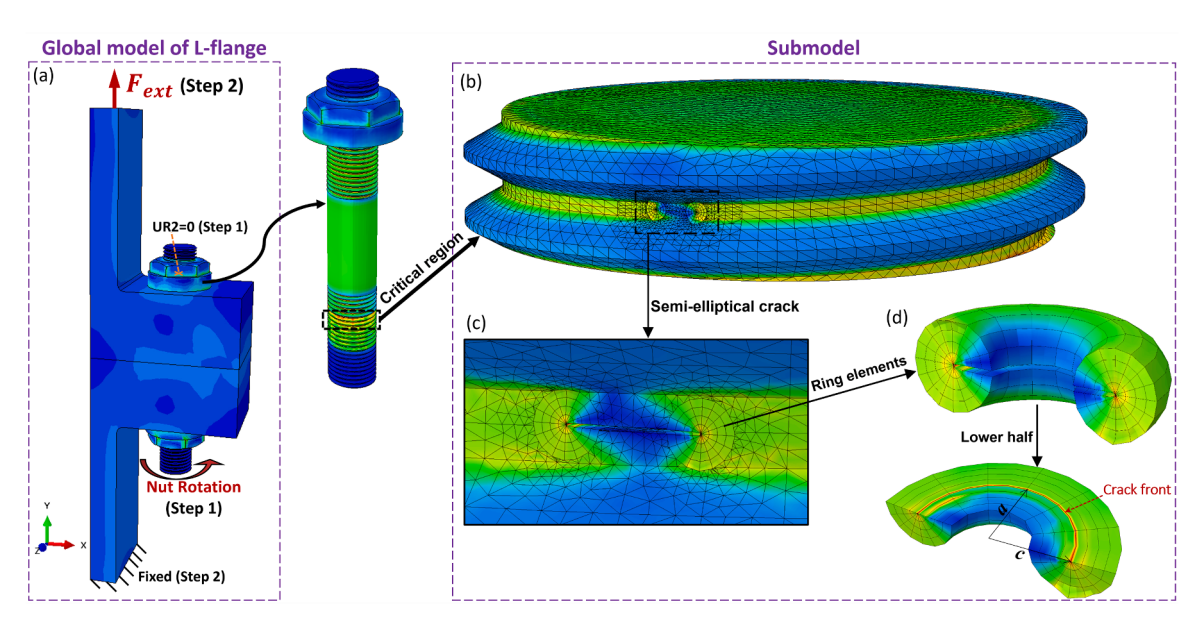


Fig. 3. Details of the 3D FE simulation: (a) BCs applied to the global model of the L-flange connection during the stud preloading (Step 1) and the external loading (Step 2), (b) Submodel extracted from the critical region of the stud, (c) Semi-elliptical crack introduced at the thread root, (d) Ring elements surrounding the crack front.

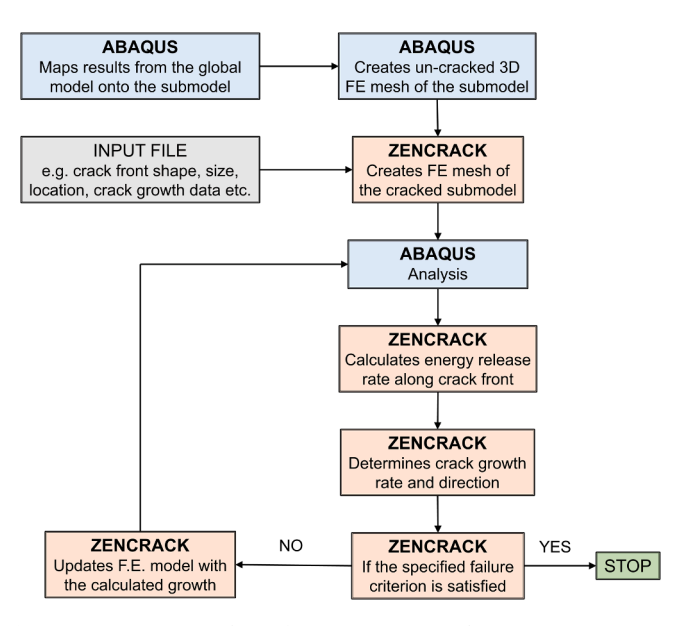


Fig. 4. Iterative procedure for 3D FCG simulation using ABAQUS and ZENCRACK.

Due to the complexity of the model and the large amount of elements, a submodelling technique was applied. As illustrated in Fig. 3b, the submodel extracted from the critical region encompassed the first engaging thread between the stud and the lower nut. This critical region selected for submodelling was determined based on the maximum stress concentration observed at the root of the first engaged thread, at the location where it is expected to initiate the first crack because of the peak tensile stress.

An un-cracked submodel was first created in ABAQUS. To ensure that the nodal locations in the submodel exactly match those in the global model, the submodel was created by copying the global model and then removing all parts except the region of interest. Using the submodel boundary condition (BC), the results from Step 2 of the global model of the L-flange were mapped onto the outer submodel's surfaces, which were cut from the global model. To verify the transfer of loading and BCs from the global to the submodel, the resultant force in the stud cross-section at the root of the first engaged thread was compared between the two models exposed to an external load of 500 kN without considering the pretension force. A difference of 1.5% was observed, indicating successful transfer of loading and BCs.

To perform the FCG analysis, the submodel was then imported into ZENCRACK, where an initial semi-elliptical crack with an aspect ratio of $a_i/c_i{=}1$ and an initial crack depth $a_i{=}1$ mm was introduced at the root of the first engaging thread between the stud and nut, as shown in Fig. 3c. The procedure of the iterative 3D FCG simulation using the remeshing technique is schematically illustrated in Fig. 4.

The maximum energy release rate was used as the criterion to predict the crack growth direction. The energy release rate was computed at each node along the crack front, and the node with the highest energy release rate determined the crack propagation direction. Subsequently, the crack growth increment was calculated, and the crack front was updated [48]. Due to potential variations in the growth increments among different nodes on the crack front, the shape of the crack front could change. The simulation continued until the crack reached a predefined length.

Wedge elements with a square root singular shape function were assigned to the crack front, arranged in a spider-web pattern as shown in Fig. 3d. Four surrounding rings of quadratic hexagonal solid elements (ABAQUS type C3D20R) were used to compute the J-integral. The mesh size was chosen based on a mesh convergence study near the crack front. It was found that a characteristic element size of 0.125 mm in the

vicinity of the crack front yields converged SIF calculations, with differences in SIF values between successive refinements remaining below 1%. The final submodel contained 89223 elements and 133146 nodes. Hard contact and frictionless conditions were assigned to the crack faces. A modified Newton-Raphson solver was adopted to submodel within the ABAOUS general static step.

Values of SIFs were obtained from the J-integral using the interaction integral method [41] as follows:

$$K_{\rm I} = \frac{E}{2(1-\lambda\nu^2)}J_{\rm int}^{\rm I} \tag{3}$$

$$K_{\rm II} = \frac{E}{2(1-\lambda\nu^2)} J_{\rm int}^{\rm II} \tag{4}$$

$$K_{\rm III} = \frac{E}{2(1+\nu)} J_{\rm int}^{\rm III} \tag{5}$$

where $J_{\rm int}$ represents the interaction integral and $\lambda{=}0$ for plane stress or $\lambda{=}1$ for plane strain. Since ratios $K_{\rm II}/K_{\rm I}$ and $K_{\rm III}/K_{\rm I}$ were both below 0.05, mode I was dominant, and only $K_{\rm I}$ was used for fatigue life calculations.

2.4. FCG prediction

A cyclic external load with a ratio of $R_{ext} = F_{ext}^{min}/F_{ext}^{max} = 0$ was applied to the flange. The crack growth rate was determined using the NASGRO equation [49], originally proposed by Foreman and Mettu [50]:

$$\frac{\mathrm{d}a}{\mathrm{d}N} = g(a) = C \left[\left(\frac{1-\gamma}{1-R_B} \right) \Delta K \right]^n \frac{\left(1 - \frac{\Delta K_{1,\text{th}}}{\Delta K_I} \right)^p}{\left(1 - \frac{K_{1,\text{max}}}{K_C} \right)^q}$$
(6)

where C, n, p and q are material-dependent parameters. $K_{\rm C}$ and $\Delta K_{\rm I,th}$ represent the critical SIF and threshold SIF range, respectively. The load ratio R_B of the stud is defined based on the internal stud force F_B as follows:

$$R_B = \frac{F_B^{min}}{F_B^{max}} \tag{7}$$

It should be noted that due to the presence of an initial preload in the stud, $F_B^{min} \neq 0$, leading to $R_B \neq R_{ext}$. The crack opening function γ , which accounts for the crack closure effect, was formulated by Newman [51] for $R_B \geq 0$ as Eq. (8):

$$\gamma = \frac{K_{Lop}}{K_{Lmax}} = \max(R_B, A_0 + A_1 R_B + A_2 R_B^2 + A_3 R_B^3)$$
 (8)

where the coefficients are defined as follows:

$$A_0 = (0.82 - 0.34\alpha + 0.05\alpha^2) \left[\cos \left(\frac{\pi}{2} \frac{\sigma_{\text{max}}}{\sigma_F} \right) \right]^{1/\alpha}$$
 (9)

$$A_1 = (0.415 - 0.071\alpha) \frac{\sigma_{\text{max}}}{\sigma_F}$$
 (10)

$$A_2 = 1 - A_0 - A_1 - A_3 \tag{11}$$

$$A_3 = 2A_0 + A_1 - 1 \tag{12}$$

where σ_F is the flow stress, defined as $\sigma_F = (S_y + S_u)/2$, and α varies between 1 for plane stress state and 3 for plane strain state. The threshold SIF range is given by:

$$\Delta K_{\text{I,th}} = \frac{\Delta K_{\text{th,0}} \sqrt{\frac{a}{a+a_0}}}{\left[\frac{1-\gamma}{(1-A_0)(1-R_B)}\right]^{1+R_BC_{th}}}$$
(13)

where $\Delta K_{th,0}$ is the threshold SIF range at $R_B=0$. The parameter a_0 is introduced to account for the effect of crack length on the threshold value in the short crack growth regime, representing an intrinsic crack length set to a constant value of 0.0381 mm [52]. The parameter C_{th} is an empirical constant.

It should be noted that the bolted connection in wind turbine is primarily subjected to high cycle fatigue. In such cases, after the initial few load cycles, the material behaviour stabilises within the elastic regime due to shakedown [40]. Therefore, the use of LEFM remains valid for modelling fatigue crack growth in this context. Also, axial and bending loads applied to the flange typically result in mode I-dominated crack propagation. However, in cases of mixed-mode loading, an effective SIF may be used instead of K_1 in Eq. (6).

2.5. S-N diagram

To generate an S-N curve, the number of cycles to failure was computed by numerically integrating the crack growth rate (Eq. (6)) using the trapezoidal rule with uniform spacing as follows:

$$N_{f} = \int_{a_{c}}^{a_{c}} \frac{1}{g(a)} da \approx \frac{a_{c} - a_{i}}{2k} \sum_{j=i+1}^{k} \left(\frac{1}{g(a_{j-1})} + \frac{1}{g(a_{j})} \right)$$
(14)

where k is the number of terms in the series. Failure of the L-flange is

reported for M30 bolts [46], making the crack initiation period relatively short compared to the overall lifetime. Therefore, a fracture mechanics-based approach provides a reasonable estimation of fatigue life for such bolts.

3. Experimental Determination of LTF for the L-Flange connection

In order to validate the FE model, the LTF at a given preload level was determined experimentally. Fig. 5a illustrates the tested L-flange, which has the same dimensions as those used in the FEA. The experiment utilised an M48 hot-dip galvanised stud with an ISR nut. The flange was mounted on an Instron 2 MN testing machine, and a hydraulic tensioner applied the preload. As preload is partially lost after tensioner removal, a higher preload than required was initially applied, reaching a pressure of 2000 bar. After tensioner removal, an external load of $F_{\rm ext}$ =550 kN was applied to the shell section of the L-flange, as shown in Fig. 5a.

3.1. Preload measurement

To measure preload, the stud was instrumented by strain gauges (SGs) glued to the unthreaded stud surface (Fig. 5b). Three SGs were positioned 120° apart around the circumference, as shown in Fig. 5c. Comparing the strain measured by SGs at 2000 bar pressure, with the expected strain calculated from the load-pressure diagram provided by the hydraulic tensioner supplier, the difference is approximately 1.6%.

The axial force and bending moments in the stud were calculated using Eq. (16) (details of calculation has been provided in Appendix):

$$\begin{bmatrix} F_B \\ M_{\chi} \\ M_{y'} \end{bmatrix} = EA \begin{bmatrix} \frac{1}{3} & \frac{1}{3} & \frac{1}{3} \\ \frac{D\sqrt{3}}{36} \left(-\cos\left(\theta + \frac{\pi}{3}\right) + \sin\left(\theta + \frac{\pi}{6}\right) \right) & \frac{D\sqrt{3}}{36} \left(-\cos\left(\theta + \frac{\pi}{6}\right) \right) & \frac{D\sqrt{3}}{36} \left(\cos\left(\theta + \frac{\pi}{3}\right) + \cos(\theta) \right) \\ \frac{D\sqrt{3}}{36} \left(\sin\left(\theta + \frac{\pi}{3}\right) + \cos\left(\theta + \frac{\pi}{6}\right) \right) & \frac{D\sqrt{3}}{36} \left(\sin(\theta) - \cos\left(\theta + \frac{\pi}{6}\right) \right) & \frac{D\sqrt{3}}{36} \left(-\sin(\theta) - \sin\left(\theta + \frac{\pi}{3}\right) \right) \end{bmatrix}. \begin{bmatrix} \varepsilon_1 \\ \varepsilon_2 \\ \varepsilon_3 \end{bmatrix}$$

$$(16)$$

assumed when the crack reaches 25% of the stud diameter, i.e., 12 mm. The material parameters used for fatigue life estimation are listed in Table 1 [38,46].

The S-N curve is described by a linear relationship between the number of cycles to failure (N_f) and the nominal stress range in a log-log plot as follows:

$$N_f = A(\Delta S^{\text{nom}})^{-m} \tag{15}$$

where $\log A$ and m and are the intercept and inverse slope of the S-N curve in the $\log \log p$ lot. The slope m is obtained via linear regression by plotting $\log N$ against $\log \sigma$, treating N_f as the dependent variable [53].

It should be noted that S-N curves obtained from experiments include both crack initiation and propagation life, whereas Eq. (14) accounts only for crack propagation, leading to a conservative prediction. However, large-diameter studs manufactured by thread rolling often contain pre-existing crack-like defects (~ 10 -100 μm) at the thread roots, as

Table 1 FCG parameters used for the fatigue life estimation.

$K_{\rm C}$ (MPa $\sqrt{ m mm}$)	С	C_{th}	$\Delta K_{\mathrm{th,0}}$ (MPa $\sqrt{\mathrm{mm}}$)	n	p	q	α
4743.4	1.231×10^{-12}	1.2	316.2	2.8	0.5	0.5	2.5

where D is the diameter of the unthreaded section and θ is the SG1 angle relative to the x' axis.

3.2. Gap measurement

To validate the FE model, the gap between the flange contact surfaces under external loading was experimentally measured using two methods. Three LVDTs¹ were mounted on one side of the flange (Fig. 6a), while the other side was coated to measure the displacement field around the flange contact surfaces by employing 2D digital image correlation (DIC). As illustrated in Fig. 6b, the side surfaces of the flanges were coated with a thin layer of white matt paint, followed by a sprayed black speckle pattern, to prepare the measurement surface for digital image correlation (DIC) analysis. A 21-megapixel camera was positioned to capture images of the flanges at both zero and maximum external loads. Polarised blue light was utilised during the test to ensure consistent illumination conditions for accurate measurements. A small reference block was attached to the upper flange to provide a reference length for the DIC analysis. The captured images were imported into the ZEISS INSPECT Correlate software, where the displacement of the flange

¹ Linear Variable Differential Transformer

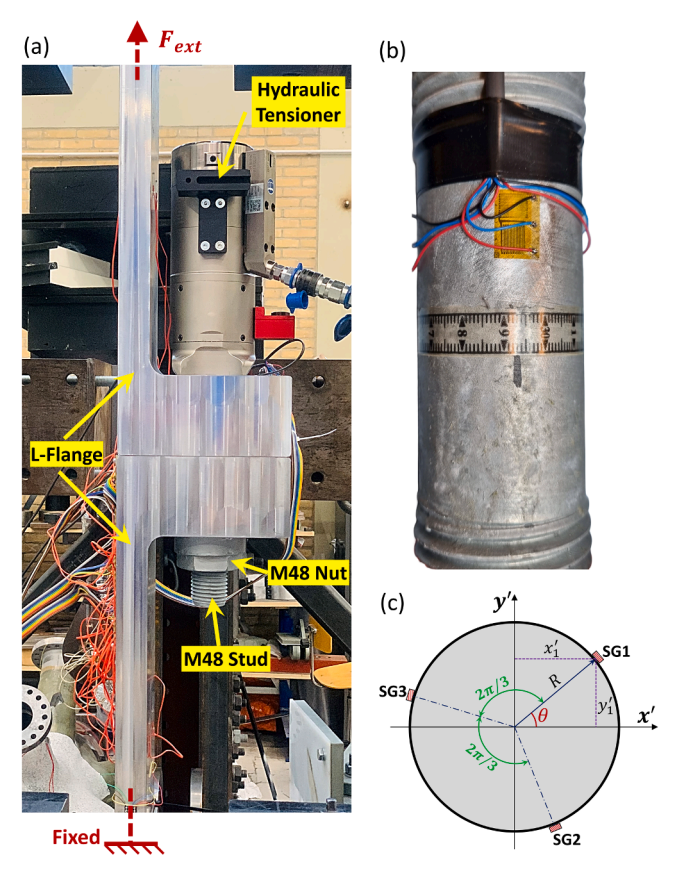


Fig. 5. (a) Experimental setup for measuring the LTF in an L-flange connection using an M48 stud and ISR nuts (b) SG glued to the unthreaded surface of the stud (c) Arrangement of SGs around the circumference of the stud, positioned at 120° interval in a local $x^{\prime}-y^{\prime}$ coordinate system.

contact surfaces was tracked and measured relative to the reference stage.

4. Validation

This section presents the validation of the numerical models developed in this study in two steps. First, the global FE model of the L-flange is validated by comparing the numerically predicted LTF with experimental measurements, ensuring that the applied BCs and preload simulation are representative of perfect L-flange behaviour. Then, the

FCG simulation is validated by comparing the SIF results with reference solutions from literature.

4.1. Validation of the FE global model of the L-flange

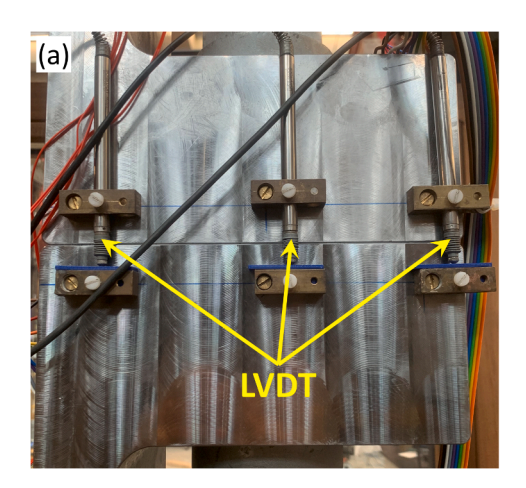
Fig. 7 presents experimental and FE results for stud force F_B , during preload application and external loading. In the experiment, the stud was initially loaded to 1387 kN. Upon removal of the tensioner, F_B decreased to 1123 kN. It can be observed that for external loads up to 260 kN, F_B remains unchanged, however, as the external load increases beyond this point, F_B starts to rise.

In the first step of the FE global model of the L-flange, a rotational displacement of 1.65 radians was applied to the nut to achieve a resultant stud preload consistent with the experimental value. In the second step, an external load of 550 kN was applied. A strong agreement is observed between the F_B values obtained from the experiment and the FEA. The maximum discrepancy between the two occurs at an external load of 550 kN, resulting in a 1.2% error.

Fig. 8 shows the gap along the flange contact surfaces under an external load of 550 kN, as measured by LVDTs and DIC, compared to FEA results. As can be seen, the gap values near the flange endpoint at X =215 mm are negative, indicating a small compressive strain. The results demonstrate good agreement between the FEA and the experimental measurements. Comparing the gap values obtained from DIC and FEM with the LVDT located at X =32 mm, the errors are 1.7% and 0.22%, respectively.

4.2. Validation of FCG simulation

To the best knowledge of the authors, no SIF data exist in the open literature for a semi-elliptical crack in a stud of an L-flange connection, considering the actual 3D geometry of threads. Therefore, to validate the adopted 3D FE simulation method for FCG, an M48 threaded rod geometry with a length-to-minor-diameter ratio of $L/D_{minor} = 1.65$ (Fig. 9a) was selected in this section, as the SIF data for this geometry have been reported by James and Mills [54], Toribio et al. [55,56] and the NASGRO software, originally developed by Mettu et al. [57]. To ensure consistency with Refs. [54-57], an additional model featuring an axisymmetric thread with zero helix angle was created. Fig. 9c illustrates the dimensionless SIF values as a function of normalised crack length for the deepest point ("A") on the crack front of a semi-elliptical crack (Fig. 9b) subjected to pure bending. The present study's results exhibit good agreement with the literature data. It is observed that discrepancies between NASGRO predictions and the current study increase for larger crack lengths. This can be attributed to NASGRO's assumption of a constant crack aspect ratio during propagation.



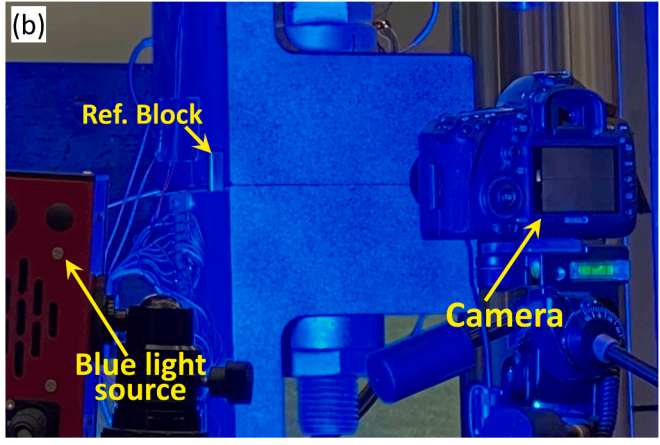


Fig. 6. Measuring the gap between the flange contact surfaces during external loading using (a) three LVDTs mounted at different positions along the flange contact surfaces (b) DIC.

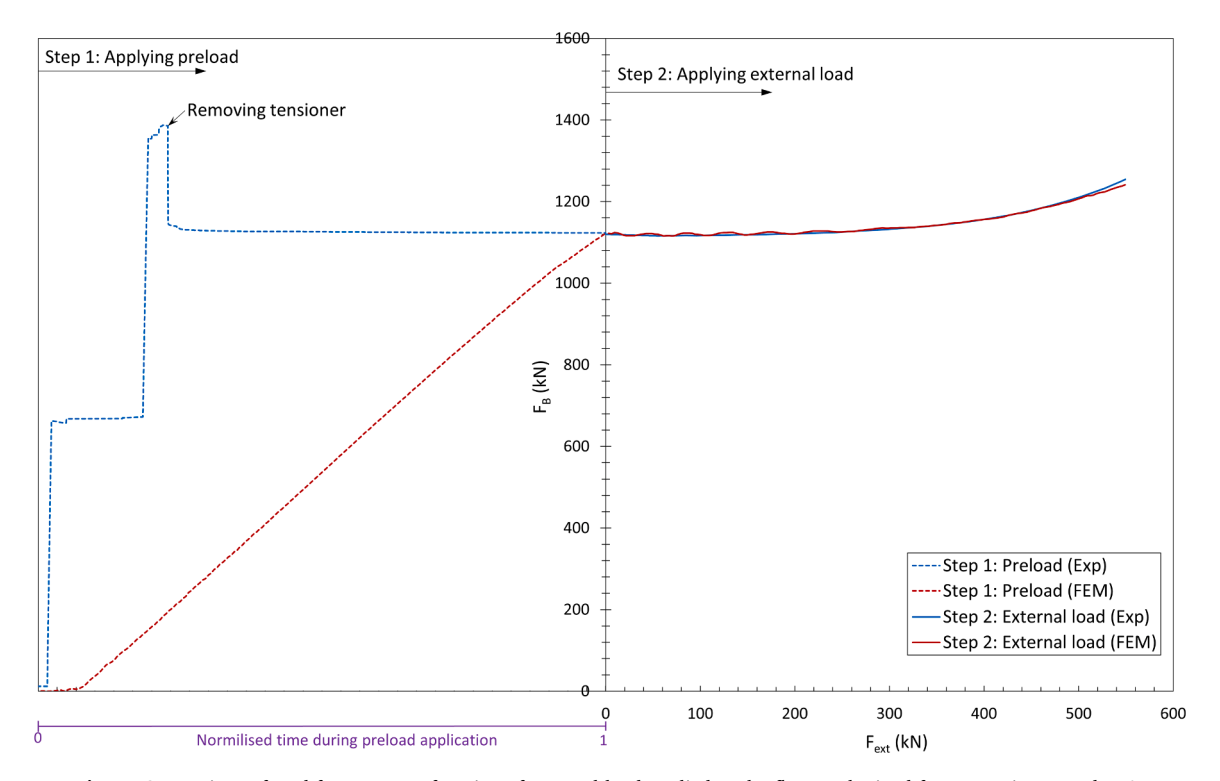


Fig. 7. Comparison of stud force F_B as a function of external load applied to the flange, obtained from experiment and FEA.

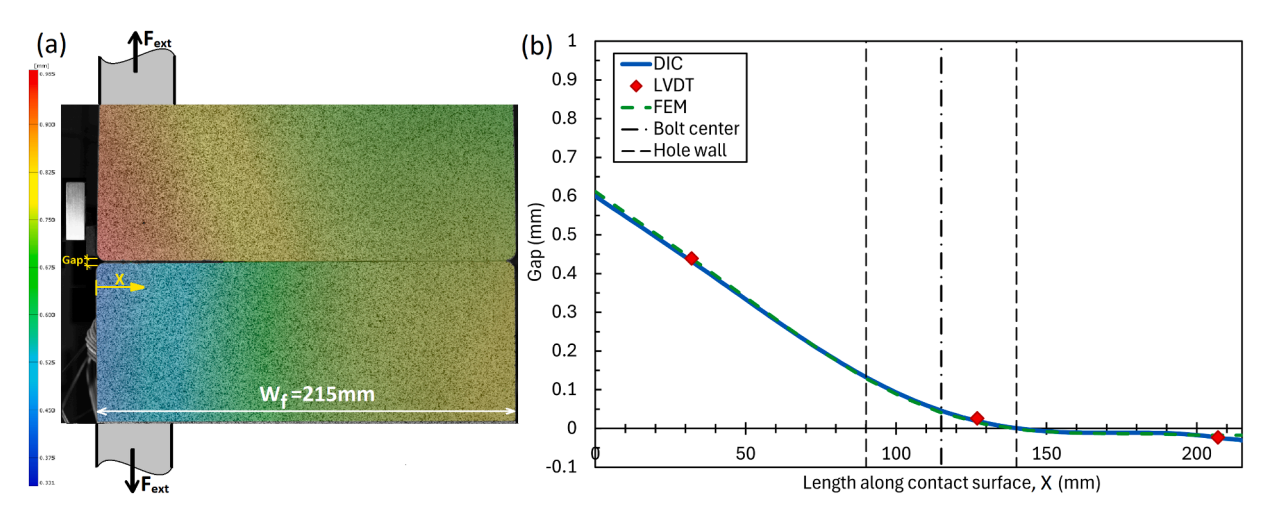


Fig. 8. (a) Distribution of vertical displacement of the flanges obtained from DIC analysis. (b) Comparison of the gap between flange contact surfaces, obtained from DIC, LVDT and FEA.

5. Results and discussion

This section presents and analyses the numerical results obtained from the FE simulations. To develop a predictive model and correlate the results for various cases, it is essential to determine the contributions of axial force and bending moment to the SIF. First, the effect of the thread helix angle on the SIF and crack front evolution is investigated for axial and bending loading. The influence of bolt preload on the LTF is then evaluated, followed by its effect on the SIF. By deriving normalised equations for both LTF and SIF, and following the methodology described in Section 2, S-N curves are generated for various preload levels. Finally, the impact of preload on fatigue life is quantified and discussed based on the predicted S-N curves.

5.1. Effect of thread helix angle and loading on the SIF and crack front shape

To investigate the effect of thread helix angle and loading on the SIF, results for a threaded rod with helical and axisymmetric threads (Fig. 9a) are compared for a crack subjected to axial force and bending moment in Fig. 10. In this section, the FCG simulation in the threaded rod was continued until the crack reached 75% of the diameter to generate a wide range of data. For short cracks, the thread helix angle has no significant effect on the SIF. However, for longer cracks under axial loading, neglecting the thread helix angle in the geometry results in a slight increase in the SIF.

It is also observed that for short cracks $(a/D_{minor} < 0.05)$, the dimensionless SIFs under axial force and bending moment are nearly identical. However, as the crack length increases, the SIF under axial force grows at a higher rate than under bending, indicating that pure

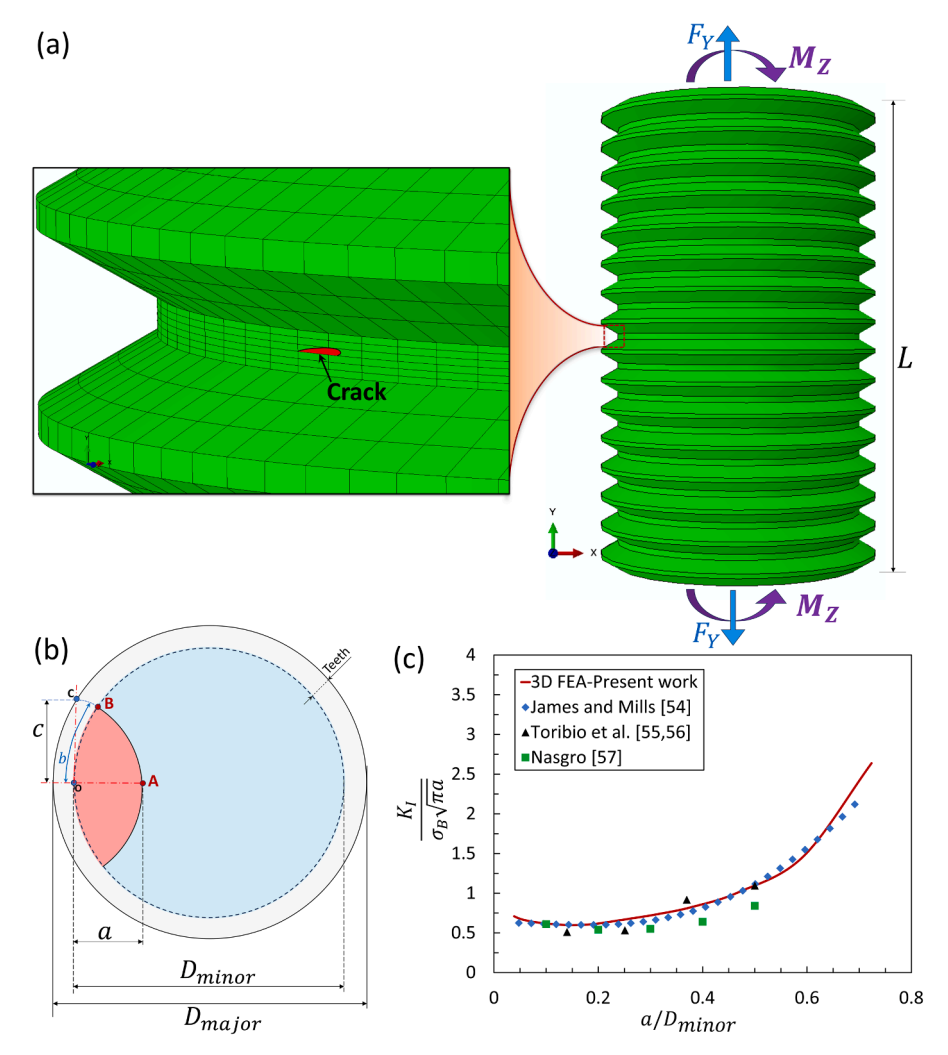


Fig. 9. (a) Geometry of an M48 axisymmetric threaded rod used for verification with a crack at the centre of the thread root. (b) Characteristic parameters of a semi-elliptical crack at the thread root. (c) Comparison of SIF values for a semi-elliptical crack subjected to bending, obtained from the present study and Refs [54–57] at the deepest point on the crack front.

bending is less damaging. This is because, in a bending-loaded specimen, part of the ligament experiences compressive loading, which does not contribute to crack opening. In addition to this, the stress gradient across the ligament in bending reduces the effective crack driving force compared to uniform tensile loading [58].

The SIF at the deepest node (point "A" in Fig. 9b) along the crack front can be expressed as Eq. (17):

$$K_I = (\sigma_A Y_A + \sigma_B Y_B) \sqrt{\pi a}$$
 (17)

where σ_A and σ_B represent stresses due to pure axial force and bending moment, respectively, and are obtained as follows:

$$\sigma_A = \frac{4F_Y}{\pi D_{\min or}^2} \tag{18}$$

$$\sigma_B = \frac{32M_Z}{\pi D_{minor}^3} \tag{19}$$

where F_Y and M_Z are axial force along the Y-axis and the bending moment around Z-axis, respectively. The geometry factors for axial and bending loading, Y_A and Y_B , also referred to as dimensionless SIFs, can be calculated for helical (HT) and axisymmetric (AT) threads as follows:

$$Y_A^{AT} = \frac{1.232 \left(\frac{a}{D_{minor}}\right)^2 + 0.01487 \left(\frac{a}{D_{minor}}\right) + 0.1356}{\left(\frac{a}{D_{minor}}\right)^3 - 1.978 \left(\frac{a}{D_{minor}}\right)^2 + 0.8268 \left(\frac{a}{D_{minor}}\right) + 0.1516}, 0.01$$

$$\leq a / D_{minor} \leq 0.75 \tag{20}$$

$$Y_{B}^{AT} = \frac{-0.2996 \left(\frac{a}{D_{minor}}\right)^{2} + 0.3268 \left(\frac{a}{D_{minor}}\right) + 0.03324}{\left(\frac{a}{D_{minor}}\right)^{3} - 1.871 \left(\frac{a}{D_{minor}}\right)^{2} + 0.8411 \left(\frac{a}{D_{minor}}\right) + 0.0349}, 0.01$$

$$\leq a / D_{minor} \leq 0.75$$
(21)

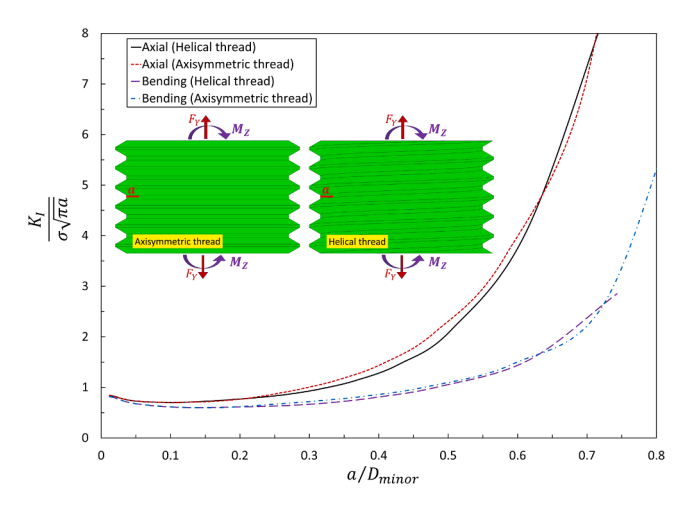


Fig. 10. Influence of thread helix angle and loading conditions on the SIF for a crack subjected to axial force and bending moment.

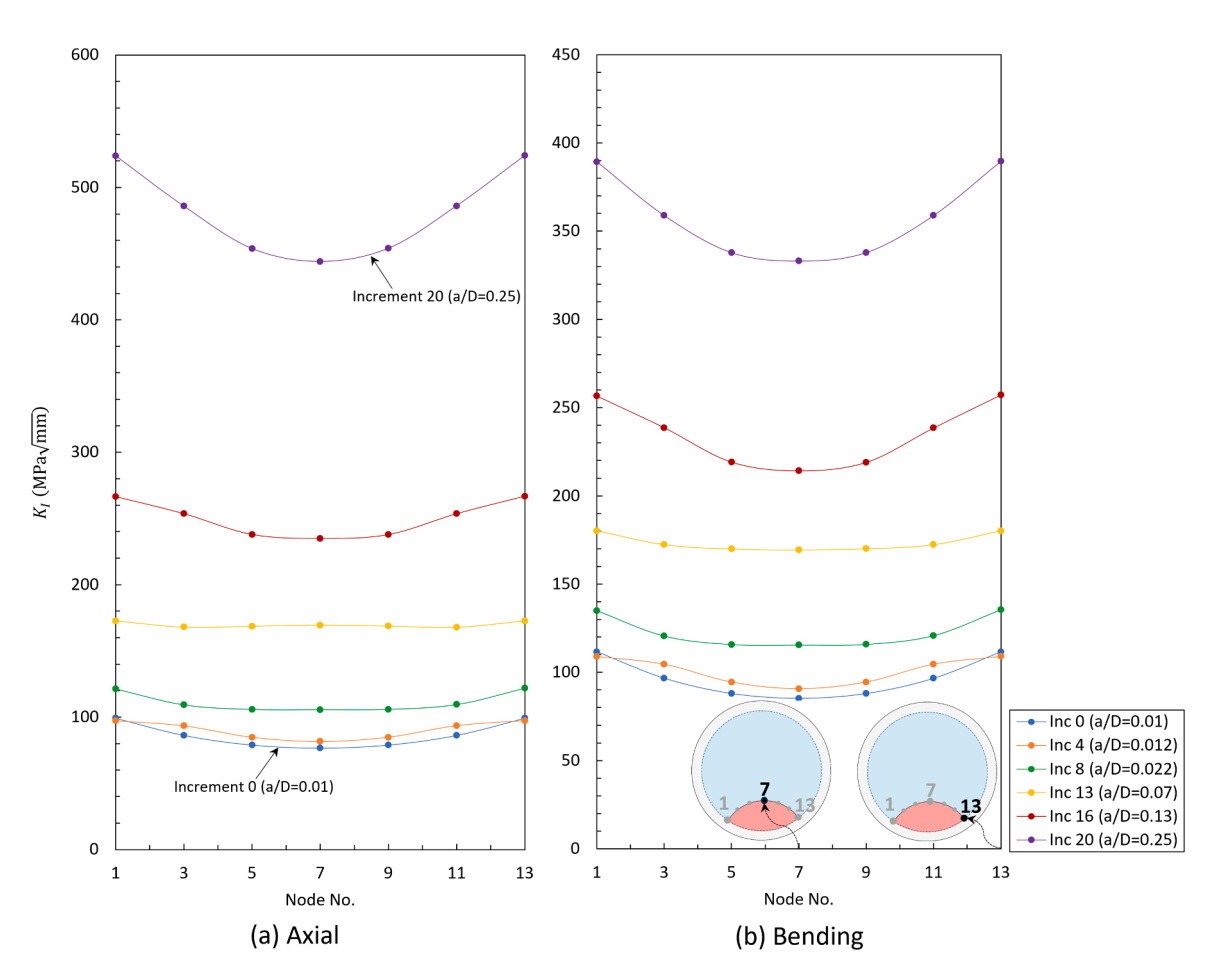
$$Y_A^{HT} = rac{-0.01435 \left(rac{a}{D_{minor}}
ight)^2 + 0.1373 \left(rac{a}{D_{minor}}
ight) + 0.04894}{\left(rac{a}{D_{minor}}
ight)^3 - 1.463 \left(rac{a}{D_{minor}}
ight)^2 + 0.4833 \left(rac{a}{D_{minor}}
ight) + 0.05438}, 0.01$$
 $\leq a / D_{minor} \leq 0.75$

$$Y_B^{HT} = \frac{-0.0369 \left(\frac{a}{D_{minor}}\right)^2 + 0.3027 \left(\frac{a}{D_{minor}}\right) + 0.07709}{\left(\frac{a}{D_{minor}}\right)^3 - 2.195 \left(\frac{a}{D_{minor}}\right)^2 + 1.097 \left(\frac{a}{D_{minor}}\right) + 0.08538}, 0.01$$

$$\leq a / D_{minor} \leq 0.75 \tag{23}$$

The SIF solutions provided in Eqs. (20) to (23) account for the crack front transition from a semi-elliptical to a straight profile for an initial crack with a/c=1 and $a=0.5\,$ mm. Fig. 11 presents the SIF distribution along the crack front in the axisymmetric thread model for various crack growth stages under pure axial force and bending moment. It is evident that the SIF at the corner nodes is higher than at the middle nodes due to stress concentration at the thread root, resulting in accelerated crack growth at the corners. Consequently, the crack front evolves from a semi-elliptical to a straight profile. Fig. 12 illustrates the history of the crack propagation profile under axial and bending loading. Initially, the half-circular crack front gradually transitions into a half-ellipse. The deepest point of the crack front grows more slowly under pure bending compared to pure axial force.

Fig. 13 depicts the variation of aspect ratios c/a and b/a, along with the straightness ratio x_B/a , for a semi-elliptical crack as a function of crack length in the axisymmetric thread model. It is seen that the transition from a semi-elliptical to a straight crack front occurs around a/D_{minor} =0.4, with this transformation occurring earlier under bending loading.



(22)

Fig. 11. SIF distribution along the crack front in the axisymmetric thread model at different crack growth stages under (a) axial and (b) bending loading.

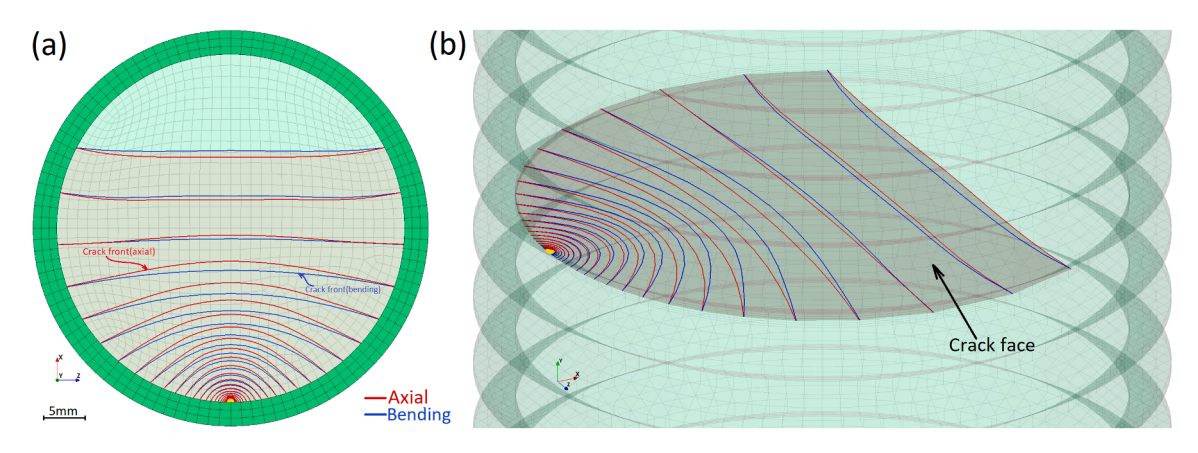


Fig. 12. Evolution of the crack front shape in the axisymmetric thread model under axial force and bending moment: (a) top view (b) 3D view.

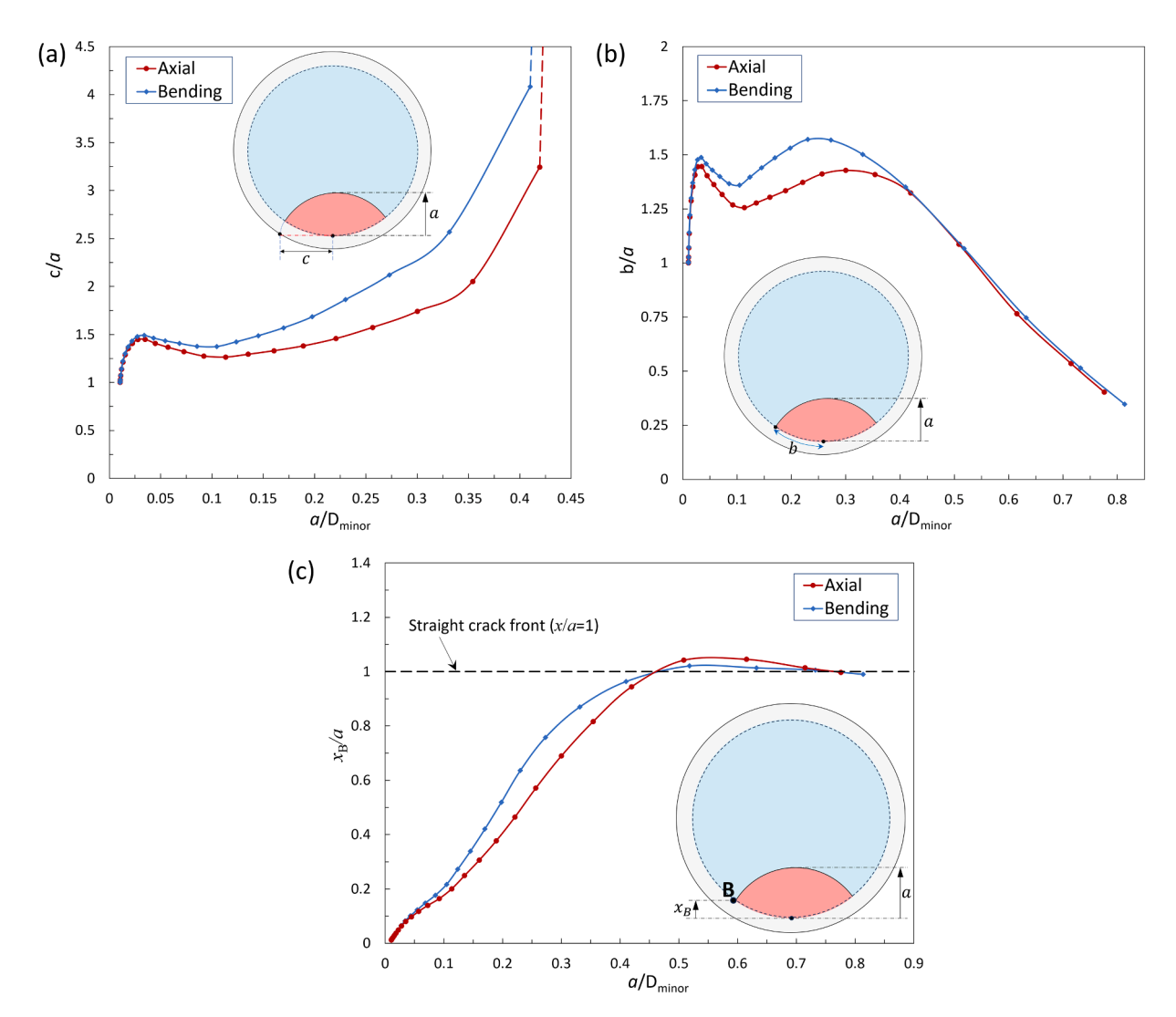


Fig. 13. Variation of crack front parameters with crack length, (a) aspect ratio c/a, (b) aspect ratio b/a, (c) straightness ratio x_B/a , for a semi-elliptical crack subjected to axial force and bending moment.

5.2. Effect of preload on LTF

Fig. 14 illustrates the variation in stud force caused by nut rotation during FEA. The secondary vertical axis represents the preload level, calculated as F_B/F_y , where $F_y=A_tS_y$ is the yield force based on the tensile-stress area A_t of the stud. As can be seen, initially, no force

develops in the stud due to the clearance between the stud and nut threads. After approximately 1.7 radians of nut rotation, the rate of increase in stud force decreases due to localised plastic deformation at the thread roots.

The stud force induced by nut rotation can be expressed as Eq. (24):

$$F_B = \frac{\Delta \text{Nut}}{1000} (83.34 \Delta \text{Nut}^4 - 489.7 \Delta \text{Nut}^3 + 895.4 \Delta \text{Nut}^2 - 615.3 \Delta \text{Nut} + 864.2)$$
(24)

$$\Delta Nut = Nut_{Rotation} - Nut_{Free}$$
 (25)

where Nut_{Free} represents the amount of free nut rotation before fully engagement between the stud and nut threads.

Fig. 15 presents the variation in stud force for different preload levels, including the case of no preload. Fig. 15a shows that upon

external load for the initiation of load transfer to the stud is shown in Fig. 15d in terms of preload level, and their relationship can be described by a four-term polynomial function as follows:

$$\frac{F_{ext}^{imi,F}}{F_{PL}} = \left(\frac{F_{PL}}{F_{y}}\right) \left[0.4682 + 1.232 \left(\frac{F_{PL}}{F_{y}}\right) - 3.395 \left(\frac{F_{PL}}{F_{y}}\right)^{2} + 2.062 \left(\frac{F_{PL}}{F_{y}}\right)^{3}\right]$$
(27)

The stud force at various preload levels can be obtained from the external load using the LTF as follows:

$$\begin{cases}
\frac{F_{B}}{F_{PL}} = 1 + \left(\frac{F_{ext} - F_{ext}^{ini,F}}{F_{u}}\right)^{2} \left[B_{1}\left(\frac{F_{ext} - F_{ext}^{ini,F}}{F_{u}}\right)^{2} + B_{2}\left(\frac{F_{ext} - F_{ext}^{ini,F}}{F_{u}}\right) + B_{3}\right] F_{ext} \ge F_{ext}^{ini,F} \\
\frac{F_{B}}{F_{PL}} = 1 F_{ext} \le F_{ext}^{ini,F}
\end{cases} (28)$$

applying an external load, the stud force initially remains unchanged (plateau region) before increasing. Fig. 15b illustrates the LTF for different preload levels, where the plateau region widens as preload increases. As the external load increases, the LTFs for various preload levels converge at a critical point (denoted as static failure), where the stress in the stud approaches its ultimate strength. Fig. 15c depicts the portion of the external load transferred to the stud, which can be determined as:

where F_u is the force corresponding to the ultimate strength of the stud. The coefficients B_i are listed in Table 2. It should be noted that the LTF coefficients provided in Table 2 were determined using least squares fitting over a preload range of 37% to 94% and for external loads up to the ultimate limit state, as shown in Fig. 15b. The validity of the LTF polynomial coefficients is within these ranges.

Fig. 15e presents the variation in the stud moment around the Z-axis (M_{ZB}) as a function of external load, which can be calculated as follows:

$$\begin{cases}
\frac{M_{Z,B}}{F_{ext}^{u} \times d_{ecc}} = \frac{\left(\frac{F_{ext} - F_{ext}^{ini,M}}{F_{u}}\right)}{C_{1}\left(\frac{F_{ext} - F_{ext}^{ini,M}}{F_{u}}\right)^{3} + C_{2}\left(\frac{F_{ext} - F_{ext}^{ini,M}}{F_{u}}\right)^{2} + C_{3}\left(\frac{F_{ext} - F_{ext}^{ini,M}}{F_{u}}\right) + C_{4}} F_{ext} \ge F_{ext}^{ini,M} \\
M_{Z,B} = 0 \ F_{ext} \le F_{ext}^{ini,M}
\end{cases}$$
(29)

$$F_{B,trans} = F_B - F_{PL} (26)$$

where F_{PL} is the stud force due to preload. As shown in Fig. 15c, beyond a certain external load threshold, denoted as $F_{ext}^{ini,F}$, the force in the stud begins to increase. As preload increases, the initiation of external load transfer to the stud occurs at a higher external load. The required

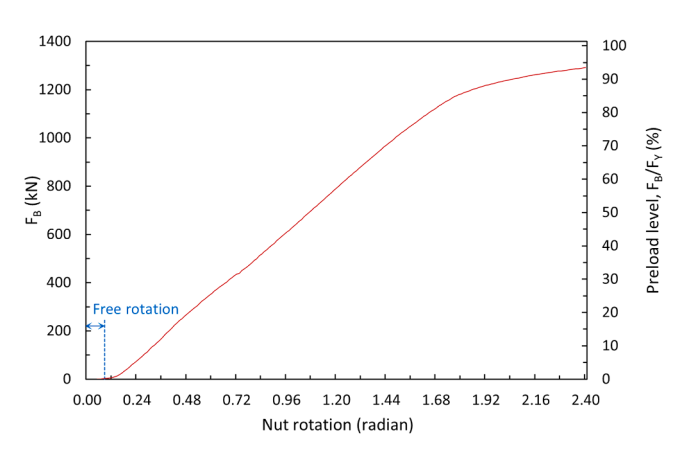


Fig. 14. Stud force and preload as a function of nut rotation.

$$\begin{split} \frac{F_{ext}^{ini,M}}{F_{PL}} &= \left(\frac{F_{PL}}{F_{y}}\right) \left[1.206 - 6.415 \left(\frac{F_{PL}}{F_{y}}\right) + 19.2 \left(\frac{F_{PL}}{F_{y}}\right)^{2} \right. \\ &\left. - 24.76 \left(\frac{F_{PL}}{F_{y}}\right)^{3} + 11.07 \left(\frac{F_{PL}}{F_{y}}\right)^{4}\right] \end{split} \tag{30}$$

where $F_{ext}^{ini,M}$ represents the external force at which the stud moment begins to increase, and F_{ext}^u denotes the external load causing static failure of the stud, i.e. $F_B \rightarrow F_u$. The coefficients C_i are provided in Table 2.

The flange gap due to the external load is another critical parameter in flange connections. Fig. 16a illustrates the gap distribution along the flange contact surfaces for different external loads at a preload level of 62%. The gap values at each load are normalised by the maximum gap observed at that load, which occurs on the flange shell side (X = 0). It can be seen that as the external load increases, the contact initiation point shifts, leading to a reduction in the contact length between the flanges. Fig. 16b presents the normalised gap for various preload levels under an external load of 400 kN. It is evident that increasing the preload extends the contact length. However, for preloads exceeding 90%, further increases have a negligible effect on contact length. The variation in contact length, $L_{\rm c}$, as a function of the ratio of external force to stud preload force ($F_{\rm ext}/F_{\rm PL}$) for different external load and preload combinations is shown in Fig. 16c and is expressed by Eq. (31):

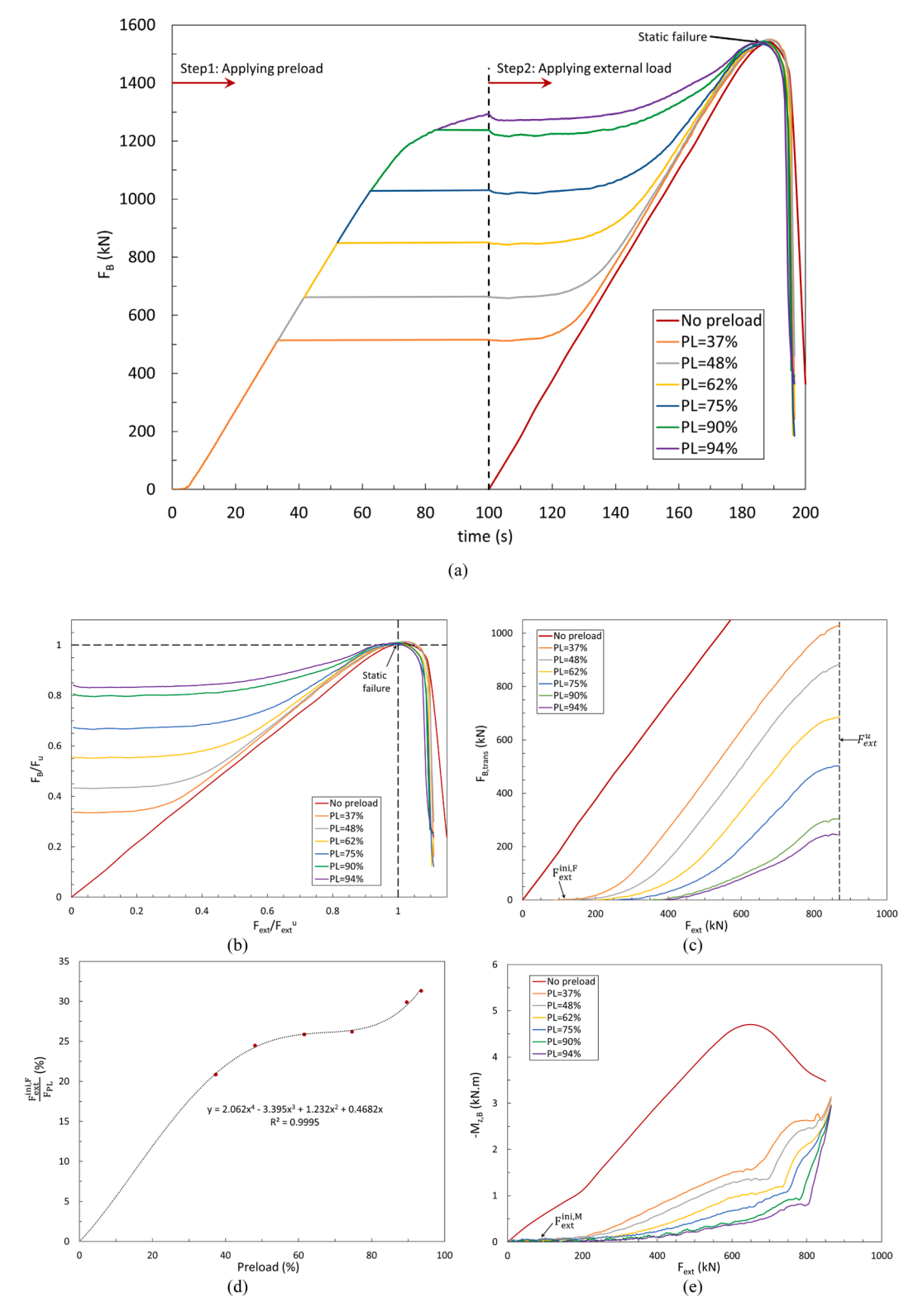


Fig. 15. (a) Evolution of stud force during preload application and external loading for various preload levels. (b) Variation of stud force with external load at different preload levels. (c) Portion of external load transferred to the stud as a function of external load. (d) Required external load for the initiation of load transfer to the stud as a function of preload. (e) Variation of stud moment around the Z-axis with external load for different preload levels.

Table 2 Coefficients of LTF.

Preload	B_1	B_2	B_3	C_1	C_2	C_3	C ₄
37 %	-22.75	-3.728	15.55	-1321	1432	-522.1	81.64
48 %	-38.23	11.62	8.997	-1079	1033	-348.3	60.96
62 %	-51.82	24.07	3.614	-232.1	40.47	-22.85	34
75 %	-45.25	21.98	1.593	224.6	-374.2	48.29	44.14
90 %	13.06	-10.77	4.72	193.3	55.16	-304.1	120
94 %	64.71	-34.91	7.278	1629	-1254	6.197	105.3

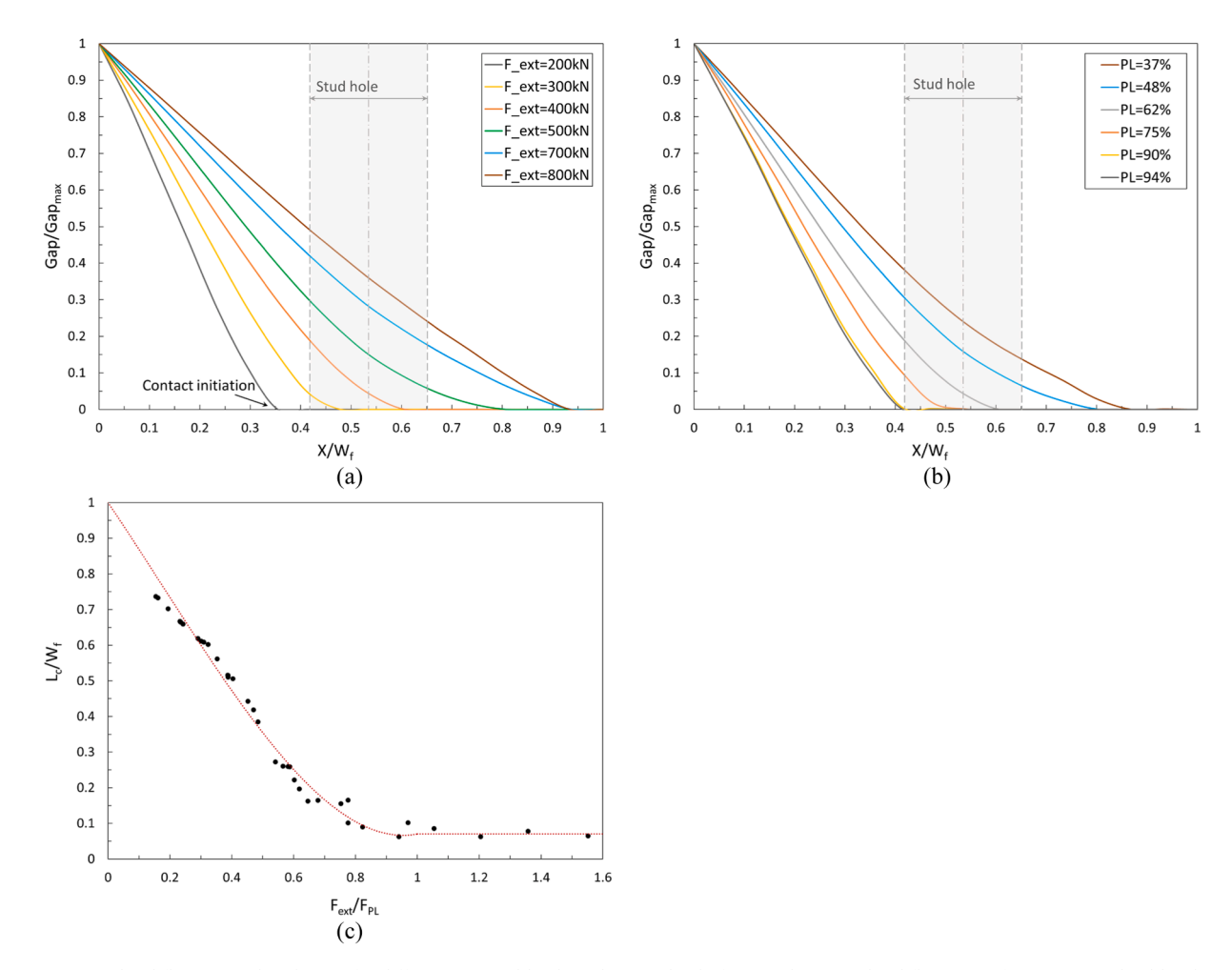


Fig. 16. (a) Normalised flange gap distribution for different external loads under a preload of 62 %. (b) Normalised flange gap for various preload levels under an external load of 400 kN. (c) Variation of contact length as a function of the ratio of external force to stud preload force F_{ext}/F_{PL} , for different load-preload combinations.

$$\begin{cases} \frac{L_{c}}{W_{f}} = 1 + \frac{F_{ext}}{F_{PL}} \left[0.7388 \left(\frac{F_{ext}}{F_{PL}} \right)^{2} - 0.3866 \left(\frac{F_{ext}}{F_{PL}} \right) - 1.2822 \right] F_{ext} \leq F_{PL} \\ \frac{L_{c}}{W_{f}} = 0.07 F_{ext} \leq F_{PL} \end{cases}$$
(31)

where $W_{\rm f}$ is the flange width along the X-axis, as shown in Fig. 8a.

5.3. Effect of preload on SIF

To develop a predictive model and correlate the results for various cases, it is essential to determine the contributions of axial force and bending moment to the SIF. The geometry factors for axial and bending loads were obtained using Eq. (17), as shown in Fig. 17a, and are stated as follows:

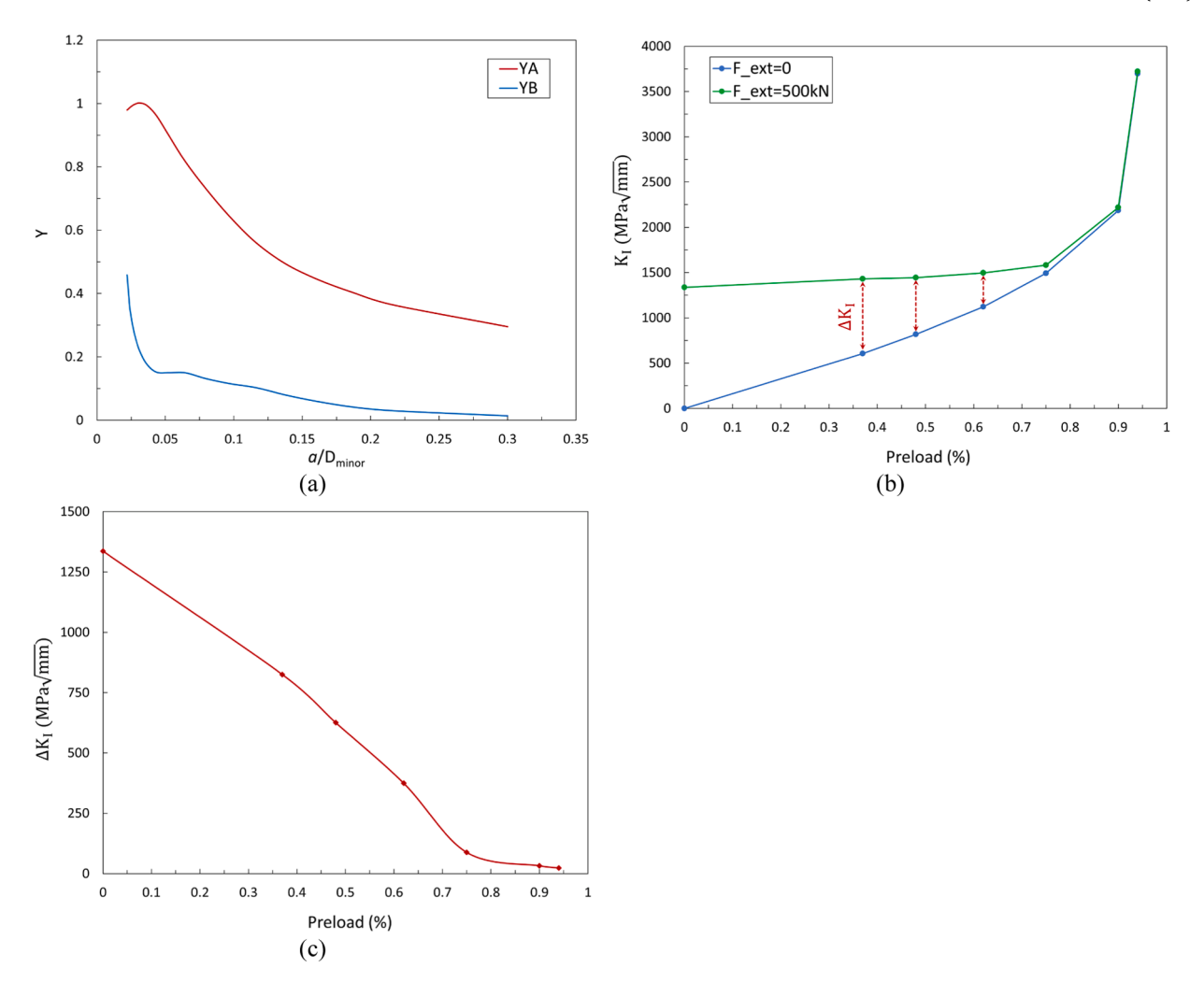


Fig. 17. (a) Geometry factors for axial and bending loading. (b) Variation of SIF with preload level for a crack of a = c = 1 mm subjected to an external load of 500 kN and 0 (c) Changes in SIF range in terms of preload level.

$$egin{align*} Y_A &= rac{1}{\left(1 - rac{a}{D_{minor}}
ight)^{3/2}} \left[rac{0.05124 \left(rac{a}{D_{minor}}
ight) + 0.001077}{\left(rac{a}{D_{minor}}
ight)^2 - 0.002986 \left(rac{a}{D_{minor}}
ight) + 0.00192}
ight], 0.02 \ &\leq a \Bigg/ D_{minor} \leq 0.3 \end{aligned}$$

SIF exhibits a slight increase, whereas the minimum SIF rises significantly due to the axial stud load induced by the preload. This results in a substantial reduction in the SIF range, as shown in Fig. 17c, which may considerably reduce the crack propagation rate and, consequently, extend the fatigue life.

5.4. Effect of preload on fatigue life (S-N curve)

Based on the results obtained in the previous sections, S-N curves for different preload levels can be generated following the sequential steps

$$Y_{B} = \frac{1}{\left(1 - \frac{a}{D_{minor}}\right)^{3/2}} \left[\frac{0.0003131 \left(\frac{a}{D_{minor}}\right) + 0.00001949}{\left(\frac{a}{D_{minor}}\right)^{3} - 0.2002 \left(\frac{a}{D_{minor}}\right)^{2} + 0.0173 \left(\frac{a}{D_{minor}}\right) - 0.0002349} \right], 0.02 \le a / D_{minor} \le 0.3$$
(33)

(32)

Employing Eqs. (32), (33) and (17), the SIF can be determined for different combinations of preload and external load. Fig. 17b illustrates the effect of preload on the SIF for an L-flange subjected to a maximum external load of 500 kN and a minimum external load of 0 kN. The results show that as the preload level increases up to 75%, the maximum

outlined in Fig. 18.

The S-N curves were obtained using a Python [59] script, allowing for efficient parameterisation. Fig 19a presents the S-N curves based on the external stress range applied to the tower shell (ΔS_{ext}). The results indicate that increasing the preload enhances fatigue life, primarily due

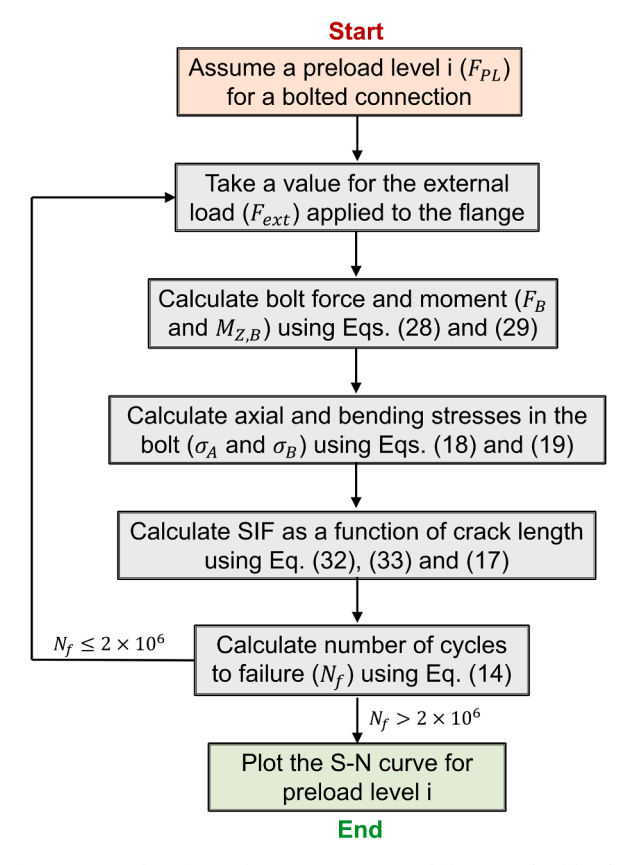


Fig. 18. Procedure for predicting S-N curves at different preload levels.

to the reduction in the SIF range, as shown in Fig. 17b and 17c. The trend in Fig. 19a reveals a nonlinear improvement in fatigue life with increasing preload, which becomes less pronounced beyond 90% of the yield preload. For instance, at an external stress range of 120 MPa, increasing the preload from 48% to 62% results in a 179% improvement in fatigue life. This effect is even more pronounced at lower stress levels-at an external stress range of 100 MPa, the same preload increase results in a 327% improvement in fatigue life. However, it is observed that for preload levels exceeding 90%, the improvement in fatigue life becomes marginal compared to levels below 90%.

Fig. 19b illustrates S-N curves based on the axial stress range in the stud (ΔS_{axial}). For comparison, an S-N curve derived from Eurocode 3 [18] is also included. The mean value for a detail category is calculated

using the following expression:

$$DC_{mean} = \gamma_M \times k_s \times DC_{Table} \tag{34}$$

where DC_{Table} is the design (characteristic) detail category provided in Eurocode 3. For a bolt that is rolled after heat treatment, this value is 71 MPa. The size factor k_s accounts for diameter effects and is given by:

$$k_{\rm s} = \left(\frac{30}{D}\right)^{0.25} \tag{35}$$

The factor γ_M adjusts the design S-N curve to estimate the mean curve and is calculated as:

$$Log(\gamma_M) = \frac{t_l \times s}{m}$$
 (36)

where t_l is one-sided tolerance limit factor calculated based on the survival probability and number of specimens and s is the standard deviation of Log(N). In several areas of applications, design codes refer to the mean minus two standard deviations, corresponding to a survival probability of 97.7%. Then, value of $t_l=2$ is used based on 20 test specimens [60], s is typically set at 0.162 for high-strength steel [19], and m=3 is the inverse slope of the S-N curve. Using these parameters, a mean detail category of 81 MPa is obtained for the M48 bolt, and the corresponding mean S-N curve is plotted in Fig. 19b.

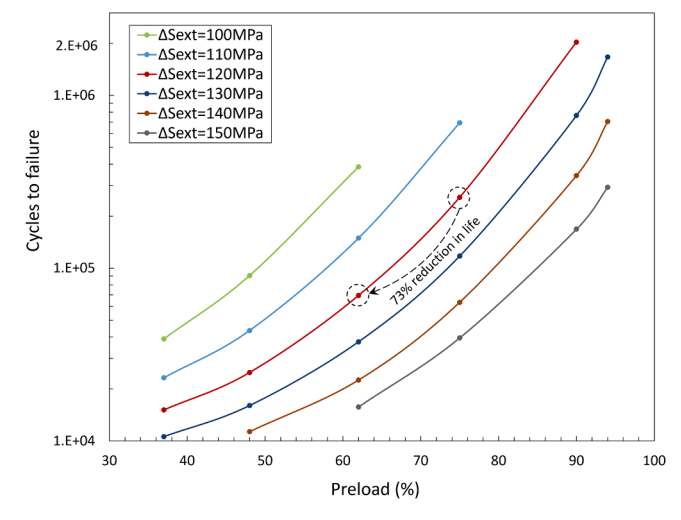


Fig. 20. Variation of fatigue life as a function of preload for different external stress ranges applied to the tower shell.

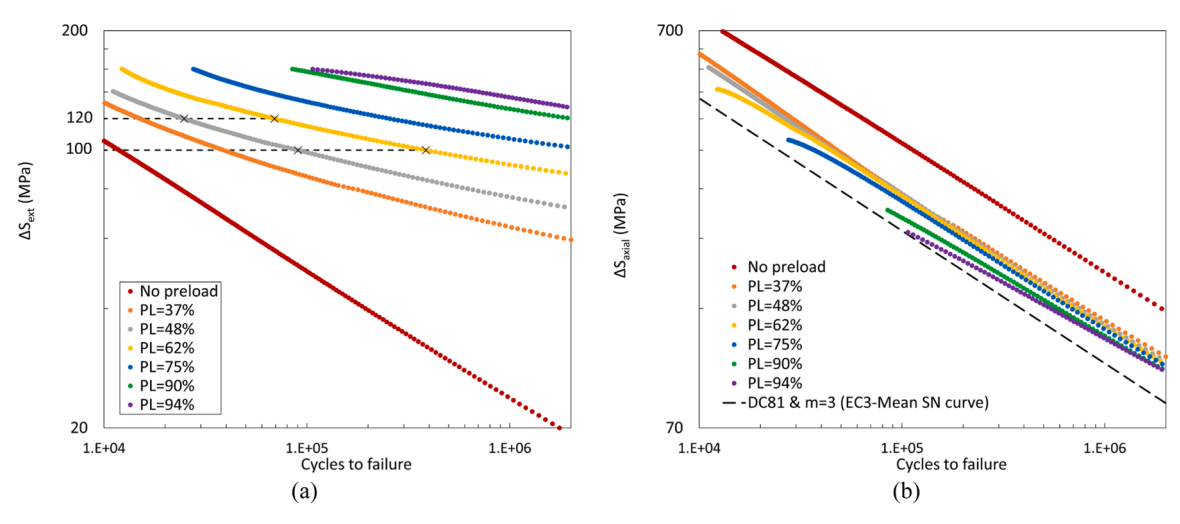


Fig. 19. S-N curves for different preload levels based on (a) the external stress range applied to the tower shell and (b) the axial stress range in the stud.

The fatigue life predicted by Eurocode 3 is lower because the values are derived from axial tests with centric loading, where no bending is present. However, in flange connections, bending occurs alongside axial loading, and as discussed in Section 5.1, bending is generally less damaging than pure axial loading.

To examine the effect of preload loss on fatigue life, Fig. 20 illustrates fatigue life as a function of preload for constant external stress ranges applied to the tower shell. It should be noted that Fig. 20 shows the effect of the final preload value after any potential causes of loss, on the fatigue life, regardless of the reasons leading to reaching that value. The results reveal that even a slight loss of preload significantly reduces fatigue life. For example, at an external stress range of 120 MPa, a reduction in preload from 75% to 62% (a 17.3% decrease) results in a 73% reduction in fatigue life. This effect becomes more pronounced at higher preload levels.

It should be noted that the nominal material parameters from the literature were used in the crack propagation model to estimate the various preload effects on fatigue lifetime. Using the measured material parameters explicitly obtained from the bolts of interest would improve the accuracy of fatigue life predictions. Additionally, an initial elliptical equivalent crack length of 1 mm was conservatively assumed in this study to account for all imperfections that might appear in the first engaged thread, thereby modelling the critical crack growth. The numerical model in this study examines a single stud within an L-flange segment, and it is widely accepted [3,16,20,33,35,36] as an effective method for addressing the governing stress state in the critical stud. The derived SIF solutions are expressed as functions of the axial force and bending moment contributions on the stud's behaviour, enabling their use in other flange designs through superposition, provided that the internal load distribution is known.

6. Conclusions and recommendations for future work

This study investigated the effect of bolt preload levels on load transfer, crack propagation, and fatigue life in a flange connection using 3D numerical fracture mechanics analysis. A methodology was developed for predicting S-N curves based on normalised solutions, involving the following sequential steps: (1) determining the bolt force and moment for a given preload level and applied shell load using LTF, (2) calculating the SIF as a function of crack length and axial/bending stresses obtained from the LTF solution, and (3) estimating the number of cycles to failure using the FCG rate equation and the computed SIF.

The findings of this study quantify the effect of preload loss for improving current fatigue design guidelines. In particular, the derived normalised solutions for LTF and SIF enable more precise fatigue life predictions under combined axial and bending loading. This, in turn, reduces excessive design conservatism. Moreover, the strong influence of preload loss on fatigue life highlights the need for accurate maintenance strategies that monitor and preserve preload levels in service, especially in critical L-flange connections.

The proposed methodology was demonstrated through a case study involving M48 L-flange connections. The key findings of this study are summarised below:

- For short cracks, the thread helix angle has no significant impact on the SIF. However, for longer cracks under axial loading, neglecting the thread helix angle slightly increases the SIF. It was also observed that the dimensionless SIFs for short cracks ($a/D_{minor} < 0.05$) under axial force and bending moment are nearly identical, but the

difference becomes more pronounced as the crack length increases. The SIF increases more quickly under axial force than under bending moment, indicating that pure bending is less damaging due to the presence of compressive loading in parts of the ligament.

- It was observed that as the preload level increases up to 75%, the maximum SIF exhibits a slight increase, while the minimum SIF rises significantly due to the axial stud load induced by the preload. This leads to a substantial reduction in the SIF range, which in turn can significantly slow crack growth and extend fatigue life.
- The effect of preload on fatigue life is more noticeable at lower external loads. Additionally, for preload levels exceeding 90%, the improvement in fatigue life becomes less pronounced compared to preload levels below 90%.
- Eurocode 3 provides a conservative estimate of fatigue life for flange connections, as it is based on axial tests without bending. However, flange connections experience bending, which is less damaging than pure axial loading.
- The results demonstrated that a small loss of preload leads to a significant reduction in fatigue life (e.g., a drop from 75% to 62% resulted in a 73% decrease), with this effect becoming more pronounced at higher preload levels.

It should be noted that the proposed methodology offers a general framework for predicting S-N curves considering preload effects, making it applicable to various flange connections. However, the specific solutions presented in this study have certain limitations. The flange geometry was idealised in the FEA analysis, and potential geometric imperfections were not considered. The analysis considers a single equivalent semi-elliptical crack at the thread root, which simplifies the problem by considering a single dominant crack. While this approach could be perceived as conservative, it paves the way for more complex consideration based on stochastic crack initiation to capture possible distributed thread damage. Moreover, the same initial crack size located at the centre of the thread root was assumed for generating S-N data across various preload levels, though in practice this may vary due to manufacturing inconsistencies. A manufacturing-induced thread tolerance deviations, surface roughness, residual stresses resulting from the thread rolling process, temperature effects, and corrosion were not included in the numerical model. While idealisation facilitates parametric exploration, incorporating these effects would enhance model realism and accuracy. Further investigations incorporating these factors, along with experimental data are required to generalise the approach to other flange geometries, as the LTF may be geometry-dependent.

CRediT authorship contribution statement

Iman Shakeri: Writing – original draft, Conceptualization, Methodology, Formal analysis, Investigation, Visualization, Validation, Software. Hagar El Bamby: Software, Investigation, Methodology. Trayana Tankova: Writing – review & editing, Supervision, Conceptualization. Milan Veljkovic: Writing – review & editing, Supervision, Project administration, Resources, Methodology, Funding acquisition, Conceptualization.

Declaration of competing interest

The authors declare that they have no known competing financial interests or personal relationships that could have appeared to influence the work reported in this paper.

Appendix

Based on the coordinate system shown in Fig. 5c, the normal stress at a point i on a circular cross section subjected to axial force, F_B , and bending moment M in the x'y' plane, can be obtained by superposition as follows:

$$\sigma_i = \sigma_{F_B,i} + \sigma_{M_{\chi'},i} + \sigma_{M_{\chi'},i} = \frac{F_B}{A_s} + \frac{M_{\chi'}y_i'}{I} + \frac{M_{\chi'}x_i'}{I}$$
(A1)

where $A_s = \pi R^2$ and $I = \pi R^4/4$ are the cross section and the second-area moment, respectively. The bending moment components about the x' and y' axes are expressed as:

$$M_{\chi} = M\cos(\theta) \tag{A2}$$

$$M_{V} = M\sin(\theta)$$
 (A3)

The positions of points 1, 2, and 3, where the SGs are located in the x'-y' coordinate system, are given by:

$$\mathbf{x}_{1}^{\prime} = R\cos(\theta), \mathbf{y}_{1}^{\prime} = R\sin(\theta) \tag{A4}$$

$$x_2' = R\cos\left(\theta - \frac{2\pi}{3}\right), y_2' = R\sin\left(\theta - \frac{2\pi}{3}\right) \tag{A5}$$

$$x_3' = R\cos\left(\theta - \frac{4\pi}{3}\right), y_3' = R\sin\left(\theta - \frac{4\pi}{3}\right) \tag{A6}$$

By substituting the strain expression $\varepsilon_i = \sigma_i/E$ and the coordinates from Eqs. (A4)-(A6) into Eq. (A1), the equation can be rewritten in terms of the strains measured by the three SGs as:

$$\begin{bmatrix} \varepsilon_{1} \\ \varepsilon_{2} \\ \varepsilon_{3} \end{bmatrix} = \begin{bmatrix} \frac{1}{EA_{s}} & \frac{R\sin(\theta)}{EI} & \frac{R\cos(\theta)}{EI} \\ \frac{1}{EA_{s}} & \frac{R\sin\left(\theta - \frac{2\pi}{3}\right)}{EI} & \frac{R\cos\left(\theta - \frac{2\pi}{3}\right)}{EI} \\ \frac{1}{EA_{s}} & \frac{R\sin\left(\theta - \frac{4\pi}{3}\right)}{EI} & \frac{R\cos\left(\theta - \frac{4\pi}{3}\right)}{EI} \end{bmatrix} . \begin{bmatrix} F_{B} \\ M_{\chi} \\ M_{y} \end{bmatrix}$$
(A7)

Substituting $I = A_s R^2/4$ and R = D/2 into Eq. (A7) gives:

Substituting
$$I = A_s R^2/4$$
 and $R = D/2$ into Eq. (A7) gives:
$$\begin{bmatrix} \varepsilon_1 \\ \varepsilon_2 \\ \varepsilon_3 \end{bmatrix} = \frac{1}{EA_s} \begin{bmatrix} 1 & \frac{8\sin(\theta)}{D} & \frac{8\cos(\theta)}{D} \\ 1 & \frac{8\sin(\theta - \frac{\pi}{3})}{D} & -\frac{8\cos(\theta - \frac{\pi}{3})}{D} \\ 1 & \frac{8\cos(\theta + \frac{\pi}{6})}{D} & -\frac{8\sin(\theta + \frac{\pi}{6})}{D} \end{bmatrix} . \begin{bmatrix} F_B \\ M_X \\ M_Y \end{bmatrix}$$
Using the inverse matrix, the axial force and bending moments can be determined in terms of strains as:

Using the inverse matrix, the axial force and bending moments can be determined in terms of strains as:

$$\begin{bmatrix} F_B \\ M_\chi \\ M_Y \end{bmatrix} = EA_s \begin{bmatrix} \frac{1}{3} & \frac{1}{3} & \frac{1}{3} \\ \frac{D\sqrt{3}}{36} \left(-\cos\left(\theta + \frac{\pi}{3}\right) + \sin\left(\theta + \frac{\pi}{6}\right) \right) & \frac{D\sqrt{3}}{36} \left(-\cos(\theta) - \sin\left(\theta + \frac{\pi}{6}\right) \right) & \frac{D\sqrt{3}}{36} \left(\cos\left(\theta + \frac{\pi}{3}\right) + \cos(\theta) \right) \\ \frac{D\sqrt{3}}{36} \left(\sin\left(\theta + \frac{\pi}{3}\right) + \cos\left(\theta + \frac{\pi}{6}\right) \right) & \frac{D\sqrt{3}}{36} \left(\sin(\theta) - \cos\left(\theta + \frac{\pi}{6}\right) \right) & \frac{D\sqrt{3}}{36} \left(-\sin(\theta) - \sin\left(\theta + \frac{\pi}{3}\right) \right) \end{bmatrix}.$$
(A9)

Data availability

Data will be made available on request.

References

- [1] A. Mehmanparast, S. Lotfian, S.P. Vipin, A review of challenges and opportunities associated with bolted flange connections in the offshore wind industry, Metals 10 (6) (2020) 732. https://doi.org/10.3390/met10060732.
- M. Seidel, A. Stang, F. Wegener, C. Schier, P. Schaumann, Full-scale validation of FE models for geometrically imperfect flange connections, J. Constr. Steel Res. 187 (2021) 106955, https://doi.org/10.1016/j.icsr.2021.106955.
- P. Schaumann, M. Seidel, Failure analysis of bolted steel flanges, in: Proc. Seventh Int. Symp. Struct. Failure Plast, Melbourne, Australia, 2000. Oct. https://www.stah lbau.uni-hannover.de/fileadmin/stahlbau/publications/2000 Seidel2.pdf.
- W. Weijtjens, A. Stang, C. Devriendt, P. Schaumann, Bolted ring flanges in offshorewind support structures - In-situ validation of load-transfer behaviour, J. Constr. Steel Res. 176 (2021) 106361, https://doi.org/10.1016/j.jcsr.2020.106361
- M. Seidel, On design of bolted ring-flange connections of wind turbines, PhD thesis (In German), http://refhub.elsevier.com/S0143-974X(20)30913-5/rf0120, 2001.

- [6] M. Seidel, P. Schaumann, Calculation of fatigue loads for bolts in eccentrically loaded flanges, Stahlbau 70 (7) (2001) 474-486, https://doi.org/10.1002 stab.200101660 (In German).
- H. El Bamby, I. Shakeri, T. Tankova, M. Veljkovic, The influence of high preloading forces on the behaviour of the bolt in ring flange connection, in: Nordic Steel Constr. Conf, Luleå, Sweden, 2024, https://doi.org/10.5281/zenodo.12192312.
- C. Schierl, E. Ghafoori, P. Schaumann, N. Stranghöner, D. Paluska, Yield-point controlled tightening of bolted ring flange connections, in: Proc. 33rd Int. Ocean Polar Eng. Conf, Ottawa, Canada, 2023, pp. 303-308. June, https://onepetro org/ISOPEIOPEC/proceedings/ISOPE23/All-ISOPE23/ISOPE-I-23-047/524279.
- S. Wang, Q. Su, X. Jiang, E. Ghafoori, Stability of steel columns with bolted strengthening under preload: experimental study, J. Constr. Steel Res. 190 (2022) 107119, https://doi.org/10.1016/j.jcsr.2021.107119
- A.R. Shahani, I. Shakeri, Experimental evaluation of the effect of preload on the fatigue life of bolts, Int. J. Steel Struct. 15 (3) (2015) 693-701, https://doi.org/
- R. Glienke, M. Schwarz, C. Johnston, M. Hagemann, M. Seidel, Update on the fatigue strength of large-size bolt-assemblies in steel constructions, Int. J. Offshore Polar Eng. 33 (1) (2023) 81-89, https://doi.org/10.17736/ijope.2023.jc882.

- [12] J. Maljaars, M. Euler, Fatigue S-N curves of bolts and bolted connections for application in civil engineering structures, Int. J. Fatigue 151 (2021) 106355, https://doi.org/10.1016/j.ijfatigue.2021.106355.
- [13] R. Glienke, M. Hagemann, R. Hanebeck, D. Schwerdt, C. Denkert, F. Wegener, M. Dörre, Experimental investigations of the mechanical-technological properties and fatigue strength of stainless steel bolting assemblies, in: Proc. 34th Int. Ocean Polar Eng. Conf, Rhodes, Greece, 2024, pp. 3124–3132. June, https://onepetro. org/ISOPEIOPEC/proceedings/ISOPE24/All-ISOPE24/ISOPE-1-24-443/546830.
- [14] I. Okorn, M. Nagode, J. Klemenc, S. Oman, Influence of geometric imperfections of flange joints on the fatigue load of preloaded bolts, Int. J. Press. Vessels Piping 210 (2024) 105237, https://doi.org/10.1016/j.ijpvp.2024.105237.
- [15] M. Seidel, Tolerance requirements for flange connections in wind turbine support structures, Stahlbau 87 (9) (2018) 880–887, https://doi.org/10.1002/ stab.201810050.
- [16] B.B. Ajae, S. Soyoz, Effects of preload deficiency on fatigue demands of wind turbine tower bolts, J. Constr. Steel Res. 166 (2020) 105933, https://doi.org/ 10.1016/j.jcsr.2020.105933
- [17] M. Seidel, IEC 61400-6 AMD1 background document: fatigue design for ring flange connections in wind turbine support structures, 2024. https://doi.org/10.13140 /RG 2.2.34114.08645
- [18] EN 1993-1-9, Eurocode 3: design of steel structures part 1-9: fatigue, European committee for standardization (CEN), 2005.
- [19] DNV-RP-C203, fatigue design of offshore steel structures, Det Norske Veritas, Høvik, Norway, 2023.
- [20] P. Schaumann, R. Eichstädt, Fatigue assessment of high-strength bolts with very large diameters in substructures for offshore wind turbines, in: Proc. 25th Int. Ocean Polar Eng. Conf, Kona, Hawaii, USA, 2015, pp. 260–267. June, https://onepetro.org/ISOPEIOPEC/proceedings/ISOPE15/All-ISOPE15/ISOPE-I-15-714/15124.
- [21] S. Lochan, A. Mehmanparast, J. Wintle, A review of fatigue performance of bolted connections in offshore wind turbines, Procedia Struct. Integr. 17 (2019) 276–283, https://doi.org/10.1016/j.prostr.2019.08.037.
- [22] M. Schwarz, R. Glienke, F. Wegener, M. Seidel, Fatigue assessment of eccentrically loaded flange connections in wind energy turbines, in: Proc. 33rd Int. Ocean Polar Eng. Conf., Ottawa, Canada, 2023, pp. 807–814. June, https://onepetro.org/ISOPE IOPEC/proceedings/ISOPE23/All-ISOPE23/ISOPE-1-23-116/524494.
- [23] J. Braithwaite, A. Mehmanparast, Analysis of tightening sequence effects on preload behaviour of offshore wind turbine m72 bolted connections, Energies 12 (23) (2019) 4406. https://doi.org/10.3390/en12234406.
- [24] R. Redondo, A. Mehmanparast, Numerical analysis of stress distribution in offshore wind turbine M72 bolted connections, Metals 10 (5) (2020) 689, https://doi.org/ 10.3390/met10050689.
- [25] A.R. Shahani, I. Shakeri, H.M. Kashani, Fatigue life estimation of bolts in flanges of a reinforced cylindrical shell, Modares Mech. Eng. 14 (13) (2015) 201–208. https://mme.modares.ac.ir/article-15-5808-en.html.
- [26] H.R. Lashgari, Sh. Zangeneh, Numerical and experimental failure analysis of wind turbine blade fastener, Eng. Fail. Anal. 156 (2024) 107837, https://doi.org/ 10.1016/j.engfailanal.2023.107837.
- [27] M. Dörre, R. Glienke, F. Kalkowsky, F. Wegener, W. Flügge, Numerical investigations on the influence of the nominal hole clearance on the plate resilience of high strength preloaded bolted joints, Materialwiss. Werkstofftech. 55 (12) (2024) 1687–1706, https://doi.org/10.1002/mawe.202300382.
- [28] C. Yang, Y. Huo, K. Meng, W. Zhou, J. Yang, Z. Nan, Fatigue failure analysis of platform screen doors under subway aerodynamic loads using finite element modeling, Eng. Fail. Anal. 174 (2025) 109502, https://doi.org/10.1016/j. engfailanal.2025.109502.
- [29] P. Xu, W. Guo, L. Yang, C. Yang, S. Zhou, Crashworthiness analysis and multiobjective optimization of a novel metal/CFRP hybrid friction structures, Struct. Multidisc. Optim. 67 (2024) 97, https://doi.org/10.1007/s00158-024-03795-x.
- [30] I. Okorn, M. Nagode, J. Klemenc, S. Oman, Influence of geometric imperfections of flange joints on the fatigue load of preloaded bolts, Int. J. Press. Vessels Piping 210 (2024) 105237, https://doi.org/10.1016/j.ijpvp.2024.105237.
- [31] I. Okorn, M. Nagode, J. Klemenc, S. Oman, Examining the effects on the fatigue life of preloaded bolts in flange joints: an overview, Metals 14 (8) (2024) 883, https://doi.org/10.3390/met14080883.
- [32] F. Yang, M. Veljkovic, Y. Liu, Fracture simulation of partially threaded bolts under tensile loading, Eng. Struct. 226 (2021) 111373, https://doi.org/10.1016/j. engstruct 2020 111373
- [33] F. Wegener, M. Schwarz, R. Glienke, F. Marten, M. Seidel, Numerical modelling of the force-deformation behaviour of preloaded bolts in L-flange joints, Stahlbau 89 (3) (2020) 266–281, https://doi.org/10.1002/stab.201900113 (In German).
- [34] F. Wegener, M. Seidel, R. Glienke, F. Marten, M. Schwarz, Numerical simulation of preload losses of bolts in ring flange connections, Stahlbau 89 (12) (2020) 1003–1015, https://doi.org/10.1002/stab.202000055 (In German).
- [35] L. Cheng, F. Yang, M. Seidel, M. Veljkovic, FE-assisted investigation for mechanical behaviour of connections in offshore wind turbine towers, Eng. Struct. 285 (2023) 116039, https://doi.org/10.1016/j.engstruct.2023.116039.

- [36] L. Cheng, H. Xin, M. Veljkovic, Numerical analysis of ring flange connection with defined surface area, Ce/Papers 4 (2021) 182–188, https://doi.org/10.1002/ cena 1279
- [37] A. Annoni, C. Johnston, A. Mehmanparast, Fatigue life analysis of threaded connections in offshore wind turbines, Appl. Ocean Res. 153 (2024) 104287, https://doi.org/10.1016/j.apor.2024.104287.
- [38] N. Stranghöner, C. Lorenz, M. Feldmann, S. Citarelli, W. Bleck, S. Münstermann, V. Brinnel, Brittle fracture of high-strength bolts of large diameters at low temperatures, Stahlbau 87 (1) (2018) 17–29, https://doi.org/10.1002/ stab.201810559 (In German).
- [39] P. Zhang, J. Li, Y. Zhao, J. Li, Crack propagation analysis and fatigue life assessment of high-strength bolts based on fracture mechanics, Sci. Rep. 13 (2023) 14567, https://doi.org/10.1038/s41598-023-41804-z.
- [40] R. Eichstädt, Fatigue Assessment of Large-Size Bolting Assemblies For Wind Turbine Support Structures, Universität Hannover, 2019, https://doi.org/ 10.15488/5157. Ph.D. thesis.
- [41] DassaultSystèmes, ABAQUS Product Documentation: ABAQUS Analysis User's Manual, Version 2023, Dassault Systèmes, Providence, RI, 2023.
- [42] ISO 965-1, ISO general purpose metric screw threads tolerances, 2013. https://www.iso.org/standard/57778.html.
- [43] BSK07, The national board of housing, building and planning's handbook on steel structures, 2007. (in Swedish) https://www.boverket.se/globalassets/publikatione r/dokument/2007/bsk 07.pdf (accessed 20 Febuary 2025).
- [44] M. Pavlović, C. Heistermann, M. Veljković, D. Pak, M. Feldmann, C. Rebelo, L.S. da Silva, Connections in towers for wind converters, part I: evaluation of down-scaled experiments, J. Constr. Steel Res. 115 (2015) 445–457, https://doi.org/10.1016/j. jcsr.2015.09.002.
- [45] A.R. Shahani, S.M.H. Sharifi, Contact stress analysis and calculation of stress concentration factors at the tool joint of a drill pipe, Mater. Des. 30 (2009) 3615–3621, https://doi.org/10.1016/j.matdes.2009.02.022.
- [46] I. Shakeri, H.K. Danielsen, A. Tribhou, S. Fæster, O.V. Mishin, M.A. Eder, Effect of manufacturing defects on fatigue life of high strength steel bolts for wind turbines, Eng. Fail. Anal. 141 (2022) 106630, https://doi.org/10.1016/j. engfailanal.2022.106630.
- [47] Zentech International Limited, ZENCRACK User Manual, Version 9.3-1, Zentech International Limited, London, 2023.
- [48] A.R. Shahani, I. Shakeri, C.D. Rans, Fatigue crack growth of Al 5083-H111 subjected to mixed-mode loading, J. Braz. Soc. Mech. Sci. Eng. 42 (2020) 442, https://doi.org/10.1007/s40430-020-02527-8.
- [49] NASA, NASGRO, Fatigue Crack Growth Computer Program, Version 3.00, JSC-22267B, NASA Johnson Space Center, Houston, TX, 1999.
- [50] R.G. Forman, S.R. Mettu, Behavior of Surface and Corner Cracks Subjected to Tensile and Bending Loads in Ti-6Al-4V alloy, NASA Technical Report NASA-TM-102165, NASA Johnson Space Center, Houston, TX, 1990. https://ntrs.nasa.gov/ap i/citations/19910009960/downloads/19910009960.pdf.
- [51] J.C. Newman, A crack opening stress equation for fatigue crack growth, Int. J. Fract. 24 (1984) R131–R135. https://doi.org/10.1007/BF00020751.
- [52] H.A. Richard, M. Sander, Fatigue Crack Growth: Detect Assess Avoid, Springer, 2016, https://doi.org/10.1007/978-3-319-32534-7.
- [53] I. Shakeri, W. Wu, A. Michel, M.A. Eder, A model for modifying the S-N curve considering the effect of boundary conditions on the fatigue crack growth of welded components, Fatigue Fract. Eng. Mater. Struct. 47 (2024) 2010–2028, https://doi.org/10.1111/ffe.14270
- [54] L.A. James, W.J. Mills, Review and synthesis of stress intensity factor solutions applicable to cracks in bolts, Eng. Fract. Mech. 30 (1988) 641–654, https://doi. org/10.1016/0013-7944(88)90156-7.
- [55] J. Toribio, V. Sanchez-Galvez, M.A. Astiz, J.M. Campos, Stress intensity factor solutions for a cracked bolt under tension, bending, and residual stress loading, Eng. Fract. Mech. 39 (1991) 359–371, https://doi.org/10.1016/0013-7944(91) 90050-R
- [56] J. Toribio, V. Sanchez-Galvez, M.A. Astiz, Stress intensification in cracked shank of tightened bolt, Theor. Appl. Fract. Mech. 15 (1991) 85–97, https://doi.org/ 10.1016/0167-8442(91)90007-7
- [57] S.R. Mettu, A. de Koning, C. Lof, L. Schra, J. McMahon, R.G. Forman, Stress Intensity Factor Solutions for Fasteners in NASGRO 3.0, in: Structural Integrity of Fasteners: Second Volume, P. Toor, Ed, ASTM International, West Conshohocken, PA, 2000, https://doi.org/10.1520/STP13530S.
- [58] J. Luksch, A. Lambai, G. Mohanty, C. Pauly, F. Schaefer, C. Motz, Size effects in fatigue crack growth in confined volumes: a microbending case study on nanocrystalline nickel, Mater. Des. 241 (2024) 112880, https://doi.org/10.1016/j. matdes.2024.112880.
- [59] Python Version 3.12, Python Software Foundation, Available at, https://www.python.org/, 2023.
- [60] A.F. Hobbacher, Recommendations For Fatigue Design of Welded Joints and Components, 2nd ed. IIW Collection, Springer, 2016.